Chinese Chemical Letters 37 (2026) 112325

Contents lists available at ScienceDirect

Chinese Chemical Letters

journal homepage: www.elsevier.com/locate/cclet

# Rational Cu-based catalyst and electrolyte design for electrochemical nitrate reduction towards ammonia

Lewa Zhang[a,c], Quan Zhou[a], Chenyuan Zhu[a,b,*], Yizhao Li[a], Shihan Zhang[c,*], Fan Dong[a,d,*]

[a] Yangtze Delta Region Institute (Huzhou), University of Electronic Science and Technology of China, Huzhou 313001, China
[b] Department of Chemistry, The University of Hong Kong, Hong Kong, China
[c] Key Laboratory of Microbial Technology for Industrial Pollution Control of Zhejiang Province, College of Environment, Zhejiang University of Technology, Hangzhou 310014, China
[d] Research Center for Environmental and Energy Catalysis, Institute of Fundamental and Frontier Sciences, University of Electronic Science and Technology of China, Chengdu 611731, China

ARTICLE INFO

*Article history:*
Received 5 May 2025
Revised 24 December 2025
Accepted 24 December 2025
Available online 25 December 2025

*Keywords:*
$NH_3$ synthesis
Electrocatalytic $NO_3RR$
Cu-based catalysts
Electrolyte composition sustainable development

ABSTRACT

Ammonia ($NH_3$) is a pivotal industrial chemical extensively utilized in agricultural production, energy storage systems, and chemical manufacturing processes. However, the conventional $NH_3$ synthesis method, the Haber-Bosch process, is not only highly energy-intensive but also produces substantial greenhouse gas emissions. On the other hand, a sustainable alternative is offered by the ambient electrocatalytic nitrate ($NO_3^-$) reduction reaction ($NO_3RR$) to $NH_3$, which utilizes renewable electricity. This process not only converts $NO_3^-$ pollutants into valuable $NH_3$ but also addresses environmental concerns by effectively utilizing $NO_3^-$ waste. In this review, we focus on the electrocatalytic synthesis of $NH_3$ *via* $NO_3RR$, systematically outlining the background of $NO_3RR$, the fundamental reaction pathways, and the methods for detecting products and intermediates. We also highlight the advantages of copper (Cu)-based catalysts in this reaction. We explore various strategies to enhance Cu catalysis, including nanoparticle synthesis, facet engineering, alloying, oxidation state tuning, and single-atom dispersion. Additionally, we provide an overview of how electrolyte composition and characteristics affect $NO_3^-$ reduction efficiency and clarify the processes that underlie these effects. We delve into $NO_3RR$'s challenges and the likelihood of $NH_3$ synthesis in the future. The goal of this work is to shed light on how to achieve environmental sustainability and create more effective $NH_3$ synthesis strategies.

© 2026 Published by Elsevier B.V. on behalf of Chinese Chemical Society and Institute of Materia Medica, Chinese Academy of Medical Sciences.

## 1. Introduction

Ammonia ($NH_3$) is an essential industrial chemical utilized in numerous fields [1,2]. As the main ingredient in nitrogen-based fertilizers, it is essential to agriculture and has a direct effect on the production and security of food worldwide. In the pharmaceutical industry, $NH_3$ is a basic precursor for synthesizing a variety of drugs, including antibiotics and anticancer agents, as well as other life-science applications. Furthermore, $NH_3$ is extensively utilized in the manufacturing of fine chemicals, including rubber, plastics, dyes, and other chemical additives. Given its extensive applications, the production and supply of $NH_3$ have far-reaching implications for the global economy, environment, and human quality of life. Currently, the annual production of $NH_3$ has reached 175 million tons, and its market value is on an annual rise [3–6].

Industrial-scale $NH_3$ synthesis predominantly utilizes the Haber-Bosch process [7], which operates under essential parameters of 400–600 °C and 150–300 atm [8–10]. Several million tons of $CO_2$ are released annually as a result of this process, which uses a lot of energy [11]. With the advancement of industrialization and increasing agricultural demand, the market for $NH_3$ is expected to continue growing, driving innovations in technology and improvements in production efficiency. In this context, methods for synthesizing $NH_3$ using clean energy, including photocatalysis [12], electrocatalysis [6,13], and enzymatic catalysis [14], have garnered increasing attention. One of the most promising approaches to resolving the issues facing the present $NH_3$ business is electrochemical synthesis of $NH_3$ using electricity from renewable sources.

Two main electrochemical pathways for $NH_3$ production are commonly explored: (1) Electrocatalytic nitrogen reduction (NRR) for $NH_3$ synthesis under ambient conditions *via* cleavage of the

* Corresponding authors.
*E-mail addresses:* chenyuanzhu@fudan.edu.cn (C. Zhu), shihanzhang@zjut.edu.cn (S. Zhang), dongfan@uestc.edu.cn (F. Dong).

https://doi.org/10.1016/j.cclet.2025.112325
1001-8417/© 2026 Published by Elsevier B.V. on behalf of Chinese Chemical Society and Institute of Materia Medica, Chinese Academy of Medical Sciences.

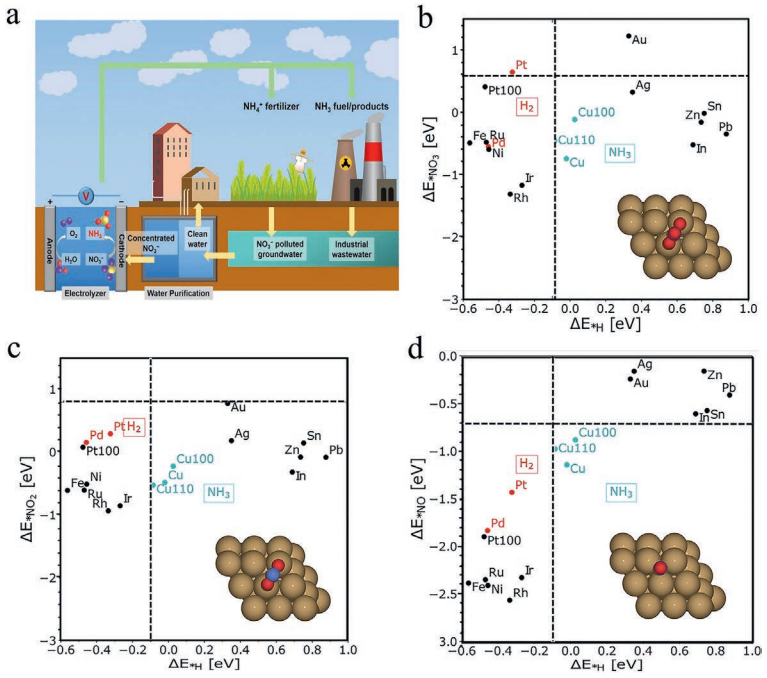



**Fig. 1.** (a) Schematic representation of the nitrogen cycle originating from $NO_3^-$ waste. Reprinted with permission [4]. Copyright 2024, Elsevier. Relationship between the adsorption energies of (b) $\Delta E_{*NO_3}$, (c) $\Delta E_{*NO_2}$, (d) $\Delta E_{*NO}$ and $\Delta E_{*H}$. (b-d) Reprinted with permission [39]. Copyright 2021, John Wiley and Sons.

strong N≡N triple bond in $N_2$. However, limited by the extremely low $N_2$ solubility and sluggish kinetics, it suffers from poor activity and selectivity [15–17]. (2) The electrochemical nitrate reduction reaction ($NO_3RR$) for $NH_3$ generation, utilizing water as the hydrogen ($H^+$) donor and nitrate anions ($NO_3^-$) as the nitrogen source. The lower bond dissociation energy of the N=O bond (204 kJ/mol) compared to that of the N≡N bond (941 kJ/mol) enables $NO_3RR$ to synthesize $NH_3$ under ambient conditions (25 °C, 1 atm) while eliminating $NO_3^-$ pollutants from wastewater without the need for secondary purification steps [18–20]. Significant benefits of this technology include affordability, great selectivity, and outstanding sustainability [21]. $NO_3RR$ not only addresses the issue of $NO_3^-$ pollution but also enables the recovery of nitrogen resources by converting $NO_3^-$ into value-added products such as $NH_3$ (Fig. 1a) [4]. When coupled with renewable electricity, this process offers a near-zero-emission route for green $NH_3$ synthesis, aligning well with national carbon neutrality goals. As a critical bridge between pollution mitigation and resource regeneration, $NO_3RR$ holds significant potential in advancing carbon neutrality and promoting a sustainable nitrogen cycle.

$NO_3RR$ is a multi-electron and multi-proton-coupled reaction, where different reaction rates and potentials can lead to a variety of products, thereby reducing selectivity for $NH_3$. Additionally, competition between the cathodic hydrogen evolution reaction (HER) and $NO_3RR$ is frequently observed. Current research aims to develop catalysts that can efficiently convert $NO_3^-$ to $NH_3$. Various metal catalysts, such as Cu, Fe, Ni, Co, Ru, Rh, Pd, Ag, Pt, In, Bi, and Sn, have been explored [22–33]. Among them, precious metals are limited by high cost, while post-transition metals such as Bi, In, Sn are frequently employed as co-catalysts or dopants to modulate the electronic properties of the host catalyst. For example, the In-Pd pair exhibits excellent catalytic performance: ordered intermetallic InPd bimetallene isolates Pd atoms in an In matrix, down-shifts the Pd d-band center, and lowers the energy barrier of the potential-determining *NO to *NHO step, thereby delivering a Faradaic efficiency (FE) of 87.2 % for $NH_3$ formation in neutral electroreduction [34]. However, such modulation is often accompanied by trade-offs: For example, while Sn modification significantly enhances the current density and catalytic activity of Rh, it concurrently impairs N–O bond cleavage capability, resulting in increased formation of $N_2O$ and $NH_3OH^+$ [35]. Bi faces a similar trade-off. When Bi is atomically dispersed within $CuCo_2O_4$ hollow nanofibers, it boosts the FE of $NH_3$ reduction to 95.5 % by facilitating $*NO_2$ hydrogenation and accelerating $NH_3$ desorption [36]. The inherently low surface defect density, poor conductivity, and limited *H activation capacity of Bi necessitate synergistic coupling with other metals to fully unleash its catalytic potential [37,38].

In contrast, transition metals exhibit potential catalytic activity in $NO_3RR$. Compared with typical transition metals such as Fe and Ni, Cu-based catalysts demonstrate more balanced catalytic performance. Cu shows moderate adsorption strength toward key intermediates, while showing negligible affinity for *H (Figs. 1b-d). This behavior suppressed HER and facilitated $NO_3RR$ [39]. Kinetic analysis reveals that, compared with other metallic catalysts, Cu-based catalysts exhibit superior $NO_3^-$ reduction performance [40], with faster reduction kinetics in the $*NO_3^-$ to $*NO_2^-$ stage and higher $NO_3^-$ conversion efficiency [41]. Additionally, the partially filled d-orbitals of Cu are located near the Fermi level, enabling effective electronic interactions with the $\pi^*$-type lowest unoccupied molecular orbital (LUMO) of $NO_3^-$. Upon adsorption onto the Cu surface, $NO_3^-$ undergoes orbital hybridization, allowing electron donation from the Cu d-band to the vacant orbitals of $NO_3^-$. This electron transfer weakens the N–O bonds, thereby facilitating the activation [42]. Although the $NH_3$ selectivity of Cu itself still has room for improvement, its excellent structural tunability, diverse oxidation states, and well-established synthesis strategies make it one of the most representative and efficient catalytic materials in current $NO_3RR$ research. To further unlock the application potential of Cu-based catalysts, researchers have developed diverse designs focusing on electronic structure regulation and intermediate adsorption behavior. Recently, $Cu_3N$, as a Cu nitride with a unique electronic structure, has demonstrated balanced adsorption between $NO_3^-$ and $H_2O$, achieving a $NH_3$ FE of 93.1 % at −0.6 V *vs.* RHE [43]. Furthermore, a study developed a hollow square-shaped Ni-

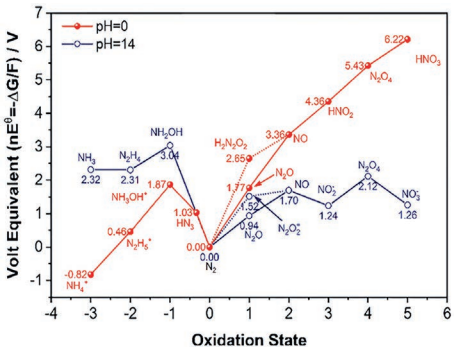



**Fig. 2.** An illustration of the different nitrogen species at pH 0 and 14 by Frost-Ebsworth. Reprinted with permission [46]. Copyright 2020, John Wiley and Sons.

doped CuO (Ni-CuO) catalyst, which modulates the reduction pathway of $NO_x$ intermediates through synergistic interaction between Cu and Ni. In a neutral electrolyte, it exhibited an $NH_3$ yield rate of 0.94 mmol $h^{-1}$ $cm^{-2}$ and selectivity exceeding 95 % [44].

In summary, Cu-based catalysts have emerged as a key research focus for efficient and selective electrochemical $NH_3$ synthesis, owing to their excellent electronic structure tunability, rich structural versatility, and strong affinity for $NO_3RR$ intermediates. In this review, we first outline the fundamental reaction processes of $NO_3RR$, including thermodynamic and kinetic considerations. Subsequently, we enumerate in detail the methods used for detecting products and intermediates. We then discuss the application of various Cu catalyst designs in $NO_3^-$ reduction, including Cu nanoparticles (NPs), facet engineering, alloys, oxidation states, and single-atom particles. Subsequently, we analyze several factors in the electrolyte that influence the catalytic performance of $NO_3RR$, including pH, various cations and anions, and $NO_3^-$ concentrations. We provide a perspective on strategies to enhance the performance of Cu-based catalysts. We explore the potential of artificial intelligence (AI)-assisted catalyst screening and address the challenges faced in this field, while also proposing the prospect of integrating this technology with other emerging reactions to synthesize high-value-added products.

## 2. Fundamentals of electrochemical $NO_3RR$ to $NH_3$

### 2.1. Thermodynamics of electrochemical $NO_3RR$

Nitrogen exhibits multiple oxidation states, with the highest oxidation state being +5 in $NO_3^-$ and the lowest being −3 in $NH_3$ [45]. The $NO_3RR$ to $NH_3$ entails an 8-electron transfer mechanism accompanied by 9 protonation events (Eq. 1), generating multiple reactive intermediates whose diversified activation pathways contribute to the increased mechanistic complexity.

$$NO_3^- + 9H^+ + 8e^- \rightarrow NH_3 + 3H_2O,\ E^0 = -0.12V\ vs.\ RHE \quad (1)$$

The Frost-Ebsworth diagram (Fig. 2) illustrates the relative stability of different nitrogen species under various conditions and their redox trends. The thermodynamic stability of nitrogen species can be analyzed through the slopes connecting different points: A higher positive slope indicates a stronger oxidation potential. Species located above the peak of adjacent points are unstable and may undergo disproportionation reactions, while those on the horizontal line coexist in equilibrium. Species at the lowest position relative to adjacent points are the most thermodynamically stable and are likely to be the final products. The generation of products in $NO_3RR$ commonly depends on reaction conditions, catalyst characteristics, and reaction routes, with $N_2$ and $NH_3$ being the predominant products [46].

### 2.2. Kinetic mechanisms of $NO_3RR$

In $NO_3RR$, many intermediates and other products are formed, complicating the reaction mechanisms and pathways. Two primary mechanisms have been proposed for $NO_3RR$: Indirect and direct mechanisms [19]. $NO_3^-$ do not directly engage in electron transport in high-concentration $NO_3^-$ electrolytes (1.0–4.0 mol/L), where the indirect pathway predominates [47]. In contrast, at low $NO_3^-$ concentrations (<1 mol/L), the direct reduction pathway becomes more prominent [48]. The direct reduction pathway can be further divided into two sub-mechanisms: Hydrogen-atom-mediated and electron-mediated pathways (Fig. 3) [49,50].

### 2.3. Pathways for $NH_3$ formation

The direct mechanism of $NO_3^-$ reduction involves adsorption and diffusion of reactants, electron transfer, and desorption of products [48]. The transformation mechanism involves two sequential electrochemical pathways: Initial conversion of $NO_3^-$ to $NO_2^-$, followed by subsequent proton-coupled electron transfer yielding $NH_3$ as the terminal product.

Adsorbed water molecules on the cathode surface undergo reduction in the hydrogen-atom-mediated pathway through the Volmer process, producing active adsorbed hydrogen (H(ad)) and hydroxide ions ($OH^-$) [51–53]. H(ad) acts as a reducing agent, reacting with adsorbed $NO_3^-$ ($NO_3^-$(ad)) to form intermediate species such as $NO_2^-$ and adsorbed nitrogen atom (N(ad)), ultimately reducing N(ad) to $NH_3$ (Eqs. 2–9). The formation of N–H bonds is favored over N–N bonds due to the presence of H(ad) [54], making $NH_3$ the dominant product [55]. It is more probable that catalysts made of metals with high affinities for H(ad) will follow the hydrogen-mediated reduction mechanism [56].

In the electron-transfer-dominated pathway for $NO_3^-$ reduction, the formation of key intermediates such as adsorbed $NO_2^-$ ($NO_2^-$(ad)) and adsorbed NO (NO(ad)) is of critical importance. The reaction initiates through $NO_3^-$ adsorption onto the catalytic surface, followed by N–O bond cleavage, reducing $NO_3^-$ to $NO_2^-$ (Eq. 10), this step is considered the rate-determining step in this pathway [57]. Subsequently, $NO_2^-$ is further reduced to form NO(ad) (Eq. 11). In a commonly observed pathway, NO(ad) reacts with protons to form adsorbed NOH (NOH(ad)) (Eq. 12). Subsequent steps involve the reduction of NOH(ad) to NHOH(ad) (Eq. 13), followed by its conversion to adsorbed hydroxylamine ($NH_2OH$(ad)) (Eq. 14), and finally to $NH_3$ (Eqs. 15 and 20) [46,58,59]. In this pathway, NHOH(ad) and $NH_2OH$(ad), formed through successive hydrogenation of NO(ad), are regarded as key intermediates in the $NH_3$ formation process. Transition metal-based catalysts, due to their unpaired d-electrons, can effectively facilitate electron transfer to the LUMO $\pi^*$ orbital of $NO_3^-$, which is one of the main reasons for their high catalytic efficiency [42]. Moreover, depending on the order of deoxygenation and hydrogenation, researchers have proposed other possible $NH_3$ formation mechanisms. For example, some studies indicate that NO(ad) can first undergo deoxygenation to generate adsorbed N(ad) (Eq. 16), which are then converted to $NH_3$ through successive hydrogenation steps (Eqs. 18–20) [57,60]. After systematically studying the reaction pathways on the Cu(111) surface, Hu *et al.* proposed a more favorable pathway involving NOH(ad) as a key intermediate: NO(ad) is first hydrogenated to form NOH(ad), which is further hydrogenated to NHOH(ad), followed by dehydration to generate NH(ad) (Eq. 17), and finally converted to $NH_3$ through successive hydrogenation steps (Eqs. 19 and 20) [61]. This pathway exhibits favorable thermodynamic and kinetic advantages and is considered the most probable $NO_3^-$ reduction pathway on the Cu(111) surface.

The transition of $NO_3^-$ to $NH_3$ undergoes multiple reduction steps and different intermediate products, and there is a

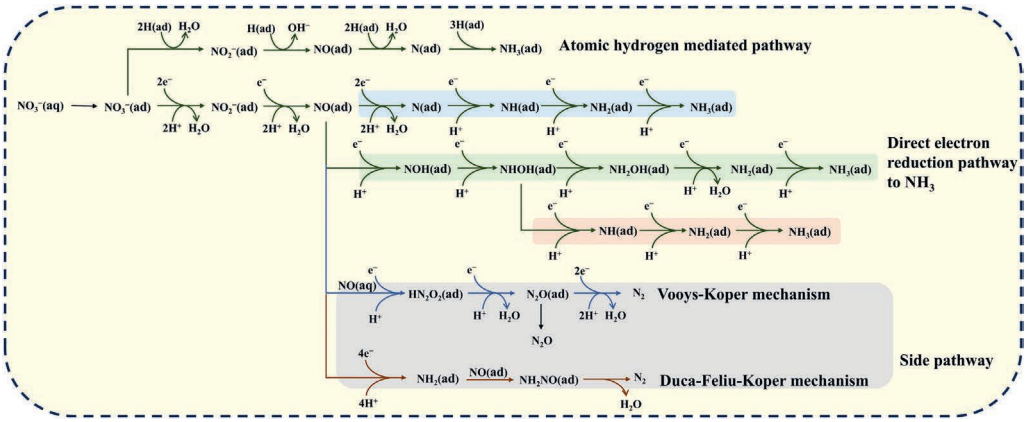



**Fig. 3.** Schematic diagram of the $NO_3RR$ mechanism.

great probability that by-products will be generated. For example, $NH_2OH(ad)$ may desorb to produce free hydroxylamine molecules. In the Vooys-Koper pathway, NO(ad) reacts with NO(aq) to form hyponitrous acid ($HN_2O_2$), which is subsequently reduced to nitrous oxide ($N_2O$), and eventually converted to $N_2$ (Eqs. 21–23) [62–65]. The Duca-Feliu-Koper mechanism is also another representative pathway for $N_2$ formation (Eqs. 24–27) [66].

$$H_2O + e^- \rightarrow H(ad) + OH^- \quad (2)$$

$$NO_3^-(aq) \rightarrow NO_3^-(ad) \quad (3)$$

$$NO_3^-(ad) + 2H(ad) \rightarrow NO_2^-(ad) + H_2O \quad (4)$$

$$NO_2^-(ad) + H(ad) \rightarrow NO(ad) + OH^- \quad (5)$$

$$NO(ad) + 2H(ad) \rightarrow N(ad) + H_2O \quad (6)$$

$$N(ad) + H(ad) \rightarrow NH(ad) \quad (7)$$

$$NH(ad) + H(ad) \rightarrow NH_2(ad) \quad (8)$$

$$NH_2(ad) + H(ad) \rightarrow NH_3(ad) \quad (9)$$

$$NO_3^-(ad) + 2H^+ + 2e^- \rightarrow NO_2^-(ad) + H_2O \quad (10)$$

$$NO_2^-(ad) + 2H^+ + e^- \rightarrow NO(ad) + H_2O \quad (11)$$

$$NO(ad) + H^+ + e^- \rightarrow NOH(ad) \quad (12)$$

$$NOH(ad) + H^+ + e^- \rightarrow NHOH(ad) \quad (13)$$

$$NHOH(ad) + H^+ + e^- \rightarrow NH_2OH(ad) \quad (14)$$

$$NH_2OH(ad) + H^+ + e^- \rightarrow NH_2(ad) + H_2O \quad (15)$$

$$NO(ad) + 2H^+ + 2e^- \rightarrow N(ad) + H_2O \quad (16)$$

$$NHOH(ad) + H^+ + e^- \rightarrow NH(ad) + H_2O \quad (17)$$

$$N(ad) + H^+ + e^- \rightarrow NH(ad) \quad (18)$$

$$NH(ad) + H^+ + e^- \rightarrow NH_2(ad) \quad (19)$$

$$NH_2(ad) + H^+ + e^- \rightarrow NH_3 \quad (20)$$

$$NO(ad) + NO(aq) + H^+ + e^- \rightarrow HN_2O_2(ad) \quad (21)$$

$$HN_2O_2(ad) + H^+ + e^- \rightarrow N_2O(ad) + H_2O \quad (22)$$

$$N_2O(ad) + e^- \rightarrow N_2O^- \quad (23)$$

$$N_2O^- + 2H^+ + e^- \rightarrow N_2 + H_2O \quad (24)$$

$$NO(ad) + 3H_2O + 4e^- \rightarrow NH_2(ad) + 4OH^- \quad (25)$$

$$NH_2(ad) + NO(ad) \rightarrow NONH_2(ad) \quad (26)$$

$$NONH_2(ad) \rightarrow N_2 + H_2O \quad (27)$$

In the $NO_3RR$, numerous intermediates and side products are frequently formed. These by-products often reduce the selectivity of the reaction and may lead to catalyst deactivation. Therefore, controlling the reaction pathways to minimize by-product formation and enhance $NH_3$ selectivity has become a crucial research direction in catalyst design. Cu stands out among various metals for $NO_3RR$ catalysis, primarily because its partially filled d-band lies energetically close to the $\pi^*$-LUMO of $NO_3^-$. This alignment enhances charge transfer from the Cu surface to $NO_3^-$, thereby facilitating its activation and subsequent reduction. Although pure Cu catalysts are active toward $NO_3RR$, they primarily generate $NO_2^-$, which strongly adsorbs onto the surface and tends to accumulate. Therefore, to mitigate $NO_2^-$ accumulation on the Cu surface and enhance $NH_3$ selectivity, rational modulation of Cu-based catalysts is of significant importance.

### 2.4. Fication of $NO_3RR$ products and characterization of reactive intermediates

The $NO_3RR$ involves multiple products, including $NO_2^-$, $NH_2OH$, $N_2H_4$, NO, $N_2O$, $N_2$, and $H_2$, as well as surface-adsorbed intermediates such as $*NO_3^-$, $*NO_2^-$, *NO, $*NH_2OH$, $*NH_2$, *NH, and *N. The formation and transformation pathways of these intermediates directly influence the distribution of final products. Therefore, comprehensive identification and quantification of both products and intermediates are crucial for deepening the understanding of reaction mechanisms, guiding catalyst design, and enhancing catalytic performance.

Conventional methods for product detection mainly include ultraviolet-visible (UV–vis) spectrophotometry, ion chromatography (IC), and gas chromatography (GC), which can be used to quantify reactants and several products.

Liquid products are primarily quantified using UV–vis spectrophotometry and IC. Both methods require the preparation of calibration curves relating concentration to absorbance, which are then used to determine the concentrations of analytes based on sample absorbance. In UV–vis analysis, the indophenol blue method or Nessler's reagent method is commonly employed for detecting $NH_3/NH_4^+$, with characteristic absorption peaks at 635 nm and 420 nm, respectively [67,68]; *N*-(1-naphthyl)-ethylenediamine spectrophotometry is used to detect $NO_2^-$ with an absorption peak at 540 nm [69]; $NO_3^-$ can be directly measured at 220 nm; the Watt and Chrisp method is applied for $N_2H_4$ detection with a peak at 455 nm [70]; and $NH_2OH$ can reduce $Fe^{3+}$ to $Fe^{2+}$, which then forms an orange complex with 1,10-phenanthroline, and the absorbance is detected at 510 nm [71]. IC generally allows for the detection of $NO_3^-$, $NO_2^-$, and $NH_4^+$ in solution, requiring small sample volumes, no color development, and offering reliable and straightforward results. Gaseous products such as $N_2$, NO, $N_2O$, and $H_2$ are quantified by GC [72]. The combined application of these conventional analytical techniques provides a robust foundation for comprehensive quantification of $NO_3RR$ products and mechanistic studies.

Conventional detection methods are straightforward and reliable. However, they lack the capability for real-time monitoring and effective identification of transient intermediates. Since these intermediates are typically unstable and short-lived, *in situ* characterization under actual reaction conditions is essential to gain a thorough understanding of the intermediate species on catalyst surfaces. Techniques such as *in situ* Fourier transform infrared spectroscopy (FTIR), differential electrochemical mass spectrometry (DEMS), and *in situ* Raman spectroscopy have been effectively employed to characterize these reactive intermediates.

*In situ* FTIR is an effective technique for identifying reaction intermediates adsorbed on the catalyst surface. In particular, attenuated total reflectance FTIR (ATR-FTIR) offers exceptional interfacial sensitivity, enabling molecular-level identification of species and real-time monitoring of dynamic interfacial changes during electrocatalytic processes.

Meanwhile, DEMS, as a highly sensitive *in situ* characterization technique, is widely employed for the real-time detection of volatile intermediates and products in electrochemical reactions. Its operating principle involves transporting gaseous or volatile species generated during the reaction through a hydrophilic membrane interface into a mass spectrometer, where specific molecules are identified and monitored based on their mass-to-charge ratios (*m/z*). In the context of $NO_3RR$, DEMS enables effective detection of key gaseous or volatile intermediates and products, including NO (*m/z* 30), $N_2O$ (*m/z* 44), $NH_2OH$ (*m/z* 33), and $NH_3$ (*m/z* 17), thereby providing strong support for mechanistic investigations. Despite its excellent performance in detecting gaseous and volatile species, DEMS remains limited in its ability to detect liquid-phase products such as $NO_2^-$ and $NH_4^+$. As such, it is often used in combination with complementary analytical techniques to achieve a more comprehensive product analysis.

For example, Wang *et al.* employed *in situ* FTIR to dynamically identify surface-adsorbed intermediates during the $NO_3RR$ process. In a Cu-$N_3$ single-atom catalyst system, FTIR measurements under varying potentials revealed characteristic absorption peaks corresponding to key intermediates: 1300 $cm^{-1}$ for $*NO_3$, 1228 $cm^{-1}$ for $*NO_2$, 1119 $cm^{-1}$ for $*NH_2$, and 1452 $cm^{-1}$ for $NH_4^+$ (Fig. S1a in Supporting information). The intensities of these signals evolved throughout the reaction, reflecting the transformation relationships among different intermediates. Notably, the gradual decrease in $*NO_3$ was accompanied by an increase in $*NH_2$ and $NH_4^+$, suggesting a sequential conversion pathway. Complementary DEMS analysis further confirmed the stepwise reduction of $NO_3^-$ on the catalyst surface, forming intermediates such as NO, HNO, and $NH_2OH$ before ultimately yielding $NH_3$. These findings, consistent with the FTIR data, suggest a plausible reaction pathway of $*NO \rightarrow *HNO \rightarrow *H_2NO \rightarrow *H_2NOH$ (Fig. S1b in Supporting information) [73].

In addition, *in situ* Raman spectroscopy enables real-time monitoring of molecular structures, chemical bonding states, and their evolution on the electrode surface by tracking Raman shift variations under different applied potentials. This technique is particularly effective in identifying and tracking key reaction intermediates. During the $NO_3RR$ process, *in situ* Raman spectroscopy detects characteristic vibrational bands of several representative intermediates, as well as potential-dependent surface structural changes. For instance, Raman peaks corresponding to CuO are observed under open-circuit potential, which subsequently disappear during electroreduction, indicating the reduction of CuO to metallic Cu during the $NO_3RR$ process (Fig. S1c in Supporting information) [74].

Compared with conventional Raman techniques, *in situ* shell isolated nanoparticle enhanced Raman spectroscopy (SHINERS) represents a more sensitive variant of *in situ* Raman spectroscopy. The technique employs $Au@SiO_2$ to effectively amplify the vibrational signals of molecules at the electrode surface, exhibiting excellent surface selectivity and signal enhancement capabilities. SHINERS is particularly suitable for identifying the adsorption behavior of molecules such as $NO_2^-$ and NO on different configurations, thereby providing a more detailed analysis of intermediate structures. It is known that $NO_3^-$ can bind to Cu in various ways [75,76]. For the three crystal facets of Cu(100), Cu(111), and Cu(110), researchers utilized SHINERS to analyze the behavior of adsorbed intermediates during the $NO_3RR$ process. The results indicate that all three facets exhibit similar intermediates, suggesting that they may follow the same reduction mechanism, but there are differences in the preference for the adsorption configurations of the $NO_2^-$. As shown in Figs. S1d-f (Supporting information), on the Cu(100) surface, the nitroxyl peak (O) is relatively intense, but the overall intermediate signal strength is the lowest; on the Cu(111) surface, $NO_2^-$ tends to adsorb in the nitrito configuration (I), and there is also adsorption of nitroxyl (O); on the Cu(110) surface, the signal is the strongest, with $NO_2^-$ favoring adsorption in both nitrito (I) and chelating nitrito configurations (J) [76]. These diverse adsorption configurations indicate that the $NO_3RR$ is far from a single pathway, and its mechanism is more complex than traditionally understood. It is inferred that the different adsorption configurations of the $NO_2^-$ may lead to performance differences among different crystal facets during the reduction process.

## 3. Cu electrocatalyst design for the $NO_3RR$

In the $NO_3RR$, unoptimized conventional Cu catalysts often exhibit low $NH_3$ selectivity because the uncontrollable exposure of

crystal facets and active sites prevents precise regulation of intermediate adsorption and conversion pathways, while the HER remains a strong competing reaction. To systematically enhance the activity and selectivity of Cu-based catalysts in $NO_3$RR, researchers have proposed a variety of structural optimization strategies, including the control of nanoparticle size and morphology, facet engineering, alloying, modulation of oxidation states, and the construction of single-atom catalytic sites. These approaches leverage the tunable electronic structure and interfacial properties of Cu to achieve precise control over $NO_3$RR performance. In this section, we systematically review recent advances in the rational design of Cu-based catalysts and provide mechanistic insights into their enhanced performance, aiming to deepen the understanding of the $NO_3$RR pathway for efficient $NH_3$ production.

### 3.1. Cu NPs

Due to its abundance, low cost, and excellent selectivity toward $NH_3$ production, Cu has attracted extensive attention as an electrocatalyst for the $NO_3$RR. In recent years, studies have demonstrated that the particle size and morphology of Cu-based catalysts significantly influence their catalytic activity and $NH_3$ selectivity, with smaller Cu NPs being particularly favorable for enhancing $NH_3$ yield and selectivity.

For example, Hoekx *et al.* synthesized monodisperse polycrystalline Cu NPs with diameters of 8.3, 10.0, and 11.9 nm through tuning the chain length of the phosphonic acid-based ligands. Among these, the 8.3 nm Cu NPs exhibited the best performance in $NO_3$RR, with a FE of 85.4% and a current density of approximately $-250\ mA/cm^2$ (Figs. 4a and b) [77]. While the overall reaction pathway remained unchanged across different particle sizes, the improved performance of smaller particles was primarily attributed to enhanced surface properties, including increased electrochemical surface area (ECSA) and a higher density of low-coordinated active sites. These features facilitate the adsorption and activation of $NO_3^-$ and key intermediates (*e.g.*, $NO_2^-$). However, extremely small particles may suffer from structural instability during the reaction, undergoing agglomeration, pulverization, or detachment, which eventually leads to performance degradation.

In addition, the morphology of Cu catalysts determines the dominant exposed crystal facets, thereby affecting the reaction mechanism and product selectivity. Comparative studies have demonstrated significant differences in $NH_3$ FE among various morphologies in alkaline electrolytes: Cu nanosheets (primarily exposing (111) facets) > Cu nanocubes ((100) facets) > Cu NPs (disordered crystal facets) (Figs. 4c and d) [78]. Notably, the (111) facet exhibits higher current density in the rate-determining step of $NO_3^-$ to $NO_2^-$ conversion, promoting N–O bond cleavage and intermediate transformation. The results underscore the significance of tailoring the size and morphology of Cu-based catalysts. Such modifications contribute to improved catalytic efficiency and enhanced selectivity in $NO_3$RR.

Defect engineering serves as a versatile strategy to simultaneously modulate both interfacial characteristics and electronic structure of Cu NPs. The deliberate engineering of defect-rich architectures, such as vacancy clusters and strain-inducing dislocations, emerges as a potent strategy for enhancing catalytic efficacy. Xu *et al.* prepared defect-rich Cu NPs (dr-Cu NPs) by means of *in situ* electrochemical reduction of CuO nanosheets (Fig. 3e). The defect structure further enhanced the adsorption of $NO_3^-$ and intermediates, inhibited side reactions, and exhibited superior catalytic performance compared to defect-free nanosheets [79]. Similarly, Zhou *et al.* constructed a Cu@CuTCNQ composite *via* an *in situ* electrochemical reconstruction strategy, introducing a high density of Cu vacancy defects. Theoretical calculations revealed that the $V_{Cu}$-Cu site exhibits a higher local electron density induced by the Cu vacancy, which drives $NO_3^-$ to adopt a tridentate O-coordination mode (Fig. 4f). This adsorption step yields a free energy of $-0.64$ eV, markedly more exothermic than the $+0.22$ eV computed for the pristine Cu surface, and the $V_{Cu}$-Cu surface exhibits superior thermodynamic performance throughout the entire reaction pathway (Fig. 4g). As a result, the catalyst achieved a FE of 96.4% with a production rate of 144.8 $\mu mol\ h^{-1}\ cm^{-2}$ at $-0.6$ V *vs.* RHE [80]. Low-coordination (LC) atom engineering on metal surfaces represents a significant form of defect engineering. Atoms with low coordination numbers possess elevated d-band centers. This unique feature endows LC surfaces with the ability to modulate the binding strength between catalysts and specific intermediates. For example, the incorporation of LC Cu sites modulates the electron density and shifts the Cu d-band center closer to the Fermi level. This enhancement in $^*NO_2$ and $^*NO$ adsorption effectively facilitates $^*NO_2$ formation and subsequent hydrogenation, significantly reducing the energy barrier of the $^*NO_2 \rightarrow {}^*NO_2H$ step, thereby promoting the overall efficiency of $NH_3$ synthesis [81].

Doping alters the electrical structure of the catalyst and makes it easier for electrons to move from the metal to the dopant atoms, thereby enhancing $NH_3$ synthesis on Cu NPs. It also has a significant effect on the active sites' surface properties and how they interact spatially with reaction intermediates [82]. For instance, sulfur (S) doping in Cu has been shown to inhibit the production of the side-product $NO_2^-$ while enhancing the hydrogenation of $NO_3^-$ to $NH_3$. Yu *et al.* prepared S-doped Cu nanorod arrays (Cu-S NAs), where the p-orbitals of S effectively bind $H^+$ from water to form H(ad). At the same potential, the $NH_3$ FE of Cu-S NAs was higher than that of Cu NAs, while Cu-S NAs exhibited a lower $NO_2^-$ FE (Figs. 4h and i) [83]. The metal-S interface is considered a major active site for catalytic hydrogenation reactions [84], which effectively lowered the energy barrier for water dissociation to generate H(ad), promoted the hydrogenation of $NO_3^-$, and increased the selectivity of $NO_2^-$ to $NH_3$. In addition, the doping modification of Cu with boron (B) exhibits better $NH_3$ selectivity and stability in the $NO_3$RR. This is because the local electronic structure of Cu has been precisely regulated through the doping of B elements. Cu atoms have a lower electron density, which results in a positive charge characteristic. As a result, the reaction energy barrier is lowered (Fig. 4j), which makes it easier for the important intermediate to develop and raises the target product's yield [85].

### 3.2. Cu model surfaces

The significant surface complexity of polycrystalline NPs poses a key obstacle to clarifying the intrinsic link between their structure and catalytic behavior. By employing strategies such as crystal facet adjustment, researchers can design specific atomic arrangements, coordination environments, and electronic properties. These engineered surfaces enable quantitative evaluation of how interfacial configurations affect intermediate adsorption, transition-state energetics, and multi-electron transfer steps. Selective exposure of crystal facets known to exhibit higher activity toward a given reaction can thus enable precise modulation of catalytic selectivity.

Taking the Cu(100) surface as an example, it exhibits reduced barriers in both thermodynamics and kinetics when compared with the Cu(111) crystal facet. This characteristic endows the Cu(100) surface with a distinct advantage in the $NO_3$RR for $NH_3$ synthesis. Specifically, the Cu(100) demonstrates a preference for the initial adsorption of $NO_3^-$ and the first-step hydrogenation and has more advantages in the $NH_3$ synthesis, exposing more Cu(100) planes can promote the formation of $NH_3$ [86]. For instance, Ren *et al.* increased the content of Cu(100) on the surface of Cu foil through surface modification. In contrast to the initial electropolished Cu foil, the activity of $NO_3$RR was increased by

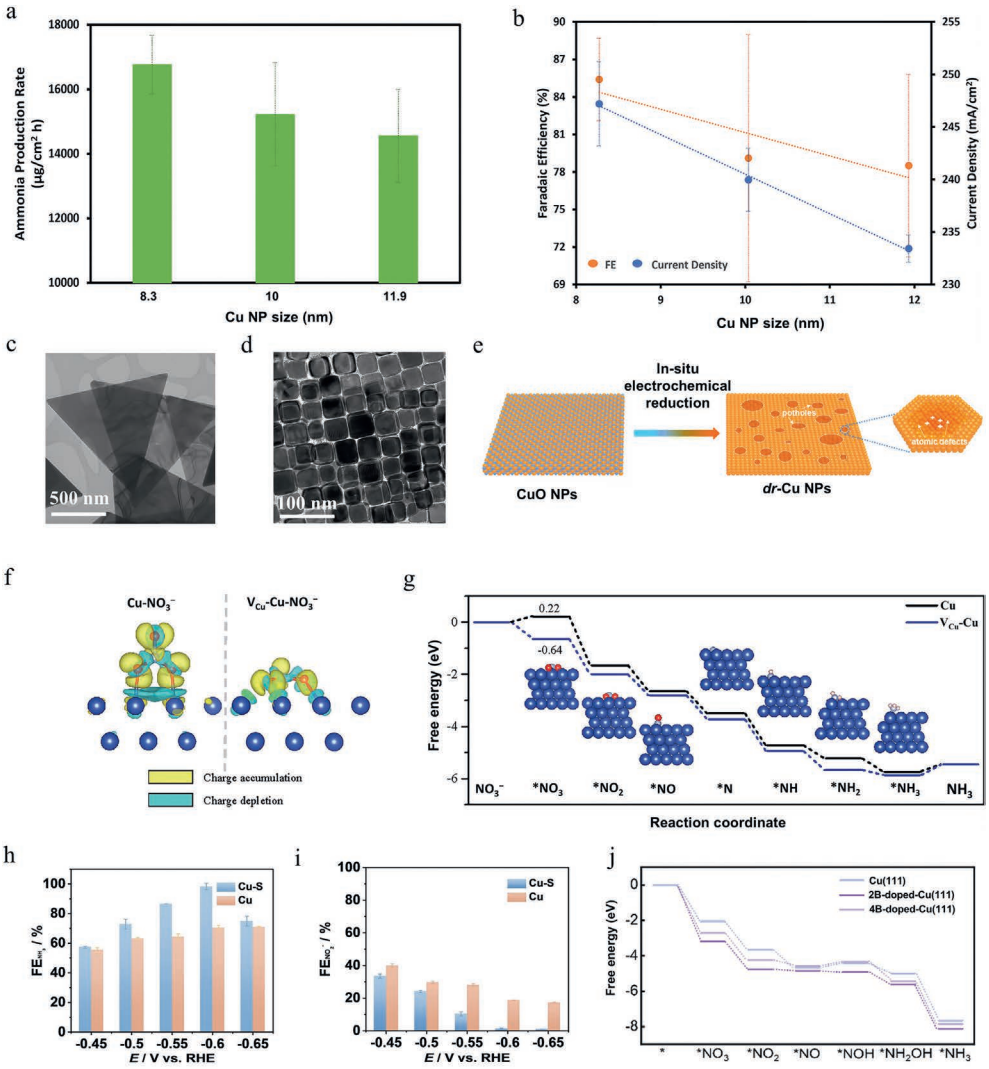



**Fig. 4.** (a) Relationship between Cu NP size and $NH_3$ production rate, and (b) the absolute current density and FE of Cu NPs with different sizes under chronoamperometry test. (a, b) Reprinted with permission [77]. Copyright 2024, American Chemical Society. (c) TEM images of Cu nanosheets and (d) nanocubes. (c, d) Reprinted with permission [78]. Copyright 2020, Elsevier. (e) Diagrammatic representation of the dr-Cu NPs' synthesis process. Reprinted with permission [79]. Copyright 2012, Royal Society of Chemistry. (f) Charge density difference between pristine Cu and $V_{Cu}$-Cu after $NO_3^-$ adsorption (cyan: electron depletion; yellow: electron accumulation). (g) Gibbs free energy diagram of $NO_3$RR on Cu and $V_{Cu}$-Cu ($U = 0$ V *vs.* RHE). (f, g) Reprinted with permission [80]. Copyright 2023, Elsevier. Comparison of (h) $NH_3$ FE and (i) $NO_2^-$ FE for Cu-S NAs and Cu NAs at different potentials. (h, i) Reprinted with permission [83]. Copyright 2024, John Wiley and Sons. (j) Gibbs free-energy diagrams of $NO_3^-$-to-$NH_3$ over Cu(111), 2B-doped-Cu(111) and 4B-doped-Cu(111), respectively. Reprinted with permission [85]. Copyright 2012, Royal Society of Chemistry.

approximately 50 %, and the FE of $NH_3$ for the modified Cu foil electrode reached 91 % at −0.2 V *vs.* RHE (Fig. 5a) [87]. However, recent research has further unveiled the significant advantages of the Cu(111) facet. Xu *et al.* utilized magneto-electrochemical deposition, harnessing the magnetohydrodynamic effect induced by magnetic fields, to successfully fabricate a Cu-based catalyst with a preferential (111) facet orientation of 94.83 %. At −0.7 V (*vs.* SCE), its $NH_3$ FE and yield markedly surpass those of conventional Cu microspheres. DFT reveals that the rate-determining step (*NO→*NOH) on this facet exhibits a free energy barrier of merely 0.89 eV, considerably lower than the 1.41 eV on the Cu(100) facet. Moreover, its more ordered atomic arrangement and reduced charge transfer resistance synergistically boost intrinsic catalytic activity [88]. This discovery challenges the traditional notion of absolute Cu(100) facet superiority, highlighting the pivotal role of coordinated facet engineering and preparation method optimization for efficient $NH_3$ synthesis.

Further studies have indicated that there is a synergistic effect between the Cu(100) and Cu(111) crystal planes: Cu(100) is beneficial for the adsorption and conversion of $NO_3^-$ to $NO_2^-$, while Cu(111) subsequently promotes the hydrogenation of $^*NO_2$ to *NOH, thereby favoring $NH_3$ formation (Fig. 5b). Owing to this tandem catalysis mechanism, the Cu nanosheets achieve an $NH_3$ FE of 88 % at 665 mA/cm$^2$, and maintain stable operation for 700 h at 365 mA/cm$^2$ [89]. Additionally, Zhao *et al.* used electrochemical deposition to prepare flower-like polycrystalline Cu (FOSP-Cu) on carbon paper, with the dominant exposed surfaces being Cu(111) and Cu(100) facets. Under neutral conditions, the enhanced catalyst realized an $NH_3$ yield of 101.4 μmol h$^{-1}$ cm$^{-2}$, coupled with an $NH_3$ FE reaching 93.91 % [90]. To summarize, the selection and optimization of Cu facets are crucial for the adsorption of intermediates and product selectivity in the $NO_3$RR process. Facet engineering provides an effective means for modulating the reaction pathway of the $NO_3$RR. The selective exposure of specific facets can enhance the catalytic activity and $NH_3$ yield, thus achieving precise control over the catalytic performance.

### 3.3. Cu-based bimetallic catalysts

The challenges of elemental Cu metal in the $NO_3$RR lie in the excessive adsorption of the $NO_2^-$ intermediate and the insufficient supply of *H. These issues limit the hydrogenation process of in-

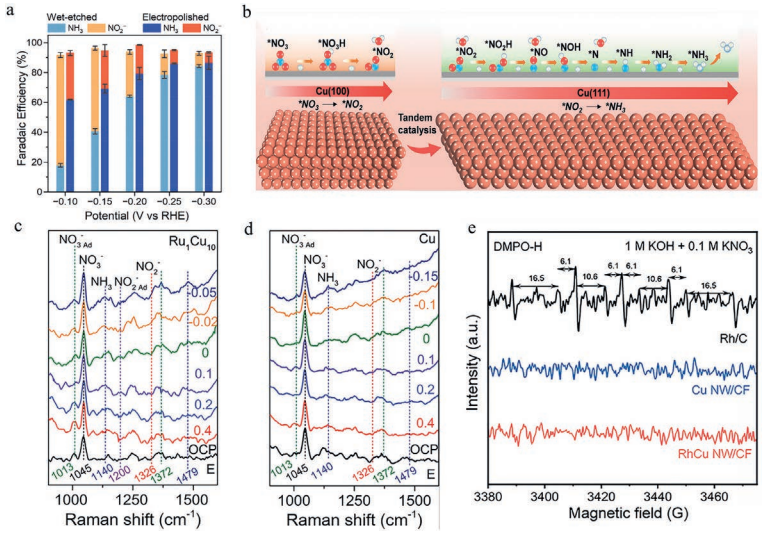



**Fig. 5.** (a) Comparison of FE for wet-etched Cu foil and electropolished Cu foil at different potentials. Reprinted with permission [87]. Copyright 2023, American Chemical Society. (b) Schematic illustration of the tandem interaction between Cu(100) and Cu(111) facets. Reprinted with permission [89]. Copyright 2023, John Wiley and Sons. *In situ* Raman spectra of (c) $Ru_1Cu_{10}$ and (d) Cu during $NO_3RR$ at selected potentials. (c, d) Reprinted with permission [93]. Copyright 2023, John Wiley and Sons. (e) Quasi *in situ* electrochemical EPR spectra of Rh/C, Cu NW/CF, and RhCu NW/CF in 1 mol/L KOH + 0.1 mol/L $KNO_3$. Reprinted with permission [96]. Copyright 2025, John Wiley and Sons.

termediates, which is particularly evident under low overpotential conditions. By alloying Cu with metals that promote the conversion of $NO_2^-$ to $NH_3$, effective relay catalysis or synergistic electrocatalysis can be achieved. The incorporation of additional metallic elements not only modulates the electronic structure and spatial configuration between metals, but also leverages multi-metallic synergistic effects to activate the reaction system, facilitate the formation and transformation of vital reaction intermediates, and thus significantly augment the catalytic performance.

Bimetallic Cu catalysts also enhance their performance by regulating the adsorption energies of intermediates in the $NO_3RR$. This modulation typically relies on heterometal modification of the Cu electronic structure. Specifically, Fe doping can induce charge redistribution at Cu sites, thereby creating functionally separated active sites: The introduction of Fe renders Cu sites electron-deficient, enhancing $NO_3^-$ adsorption, while the $Fe_3$–$N_8$ clusters constitute an electron-rich region that optimizes $NO_3^-$ adsorption and promotes *H generation. The resulting spatial charge polarization gradient drives a relay catalysis process. As reported by Liu *et al.*, the Cu-$N_3$/$Fe_3$–$N_8$ catalyst achieved a FE of 97.1 % and an $NH_3$ production rate of 18.83 mg $h^{-1}$ $mg_{cat}^{-1}$ under neutral conditions, fully highlighting the pivotal role of electronic structure modulation in bimetallic synergistic catalysis [91]. A single-phase nano-alloy catalyst (CFP-$Cu_1Ni_1$) was created by Zhang and colleagues. In a neutral electrolyte, the system demonstrated a FE of 95.7 % with a concomitant $NH_3$ production rate of 2550 μmol $h^{-1}$ $mg_{cat}^{-1}$ under −0.22 V *vs.* RHE. DFT revealed that the addition of Ni upshifted the d-band center, thereby facilitating the adsorption of intermediate while weakening the adsorption of $NH_3$. Efficient and highly selective $NO_3RR$ to $NH_3$ was achieved in the potential range above −0.24 V *vs.* RHE [92]. Gao *et al.* prepared a group of RuCu alloy catalysts ($Ru_xCu_x$/rGO). Among these alloy catalysts with different ratios, $Ru_1Cu_{10}$/rGO performed exceptionally well: At a potential of −0.05 V *vs.* RHE, it achieved an $NH_3$ generation rate of 0.38 mmol $cm^{-2}$ $h^{-1}$, while FE was as high as 98 %. Integrated experimental and *operando* Raman analyses revealed Cu preferentially drives the $NO_3^-$ to $NO_2^-$ reduction, whereas Ru selectively promotes the subsequent $NO_2^-$ to $NH_3$ conversion, constituting a tandem catalytic cycle (Figs. 5c and d). According to the DFT calculation results, the Cu-Ru solid solution catalyst precisely optimized the adsorption strength of the intermediates by synergistically regulating the d-band center (shifting it closer to the Fermi level) and interfacial charge transfer (0.77e from Cu to Ru). This approach effectively addressed the issues of intermediate accumulation caused by excessive $*NO_2^-$ desorption on pure Cu and the sluggish reduction kinetics due to strong $*NO_3^-$ adsorption on pure Ru [93]. Fang and colleagues synthesized CuCo nanosheet electrocatalysts that achieved an ampere-level current density exceeding 1 A at −0.2 V *vs.* RHE, along with an $NH_3$ FE of 100 % ± 1 %. Similar to the previous example, synergistic interplay between Cu and Co, with Co facilitating hydrogenation through *H, was demonstrated by both DFT computations and *in-situ* spectroscopy to optimize reaction intermediate coverage, thereby enhancing $NH_3$ selectivity and yield [94].

In addition to tandem catalysis, H transfer promotion serves as another important enhancement pathway. Rh exhibits excellent H adsorption-desorption properties [18,95]. In one study, RhCu alloy nanowires were supported on Cu foam (RhCu NW/CF) to construct an electrocatalyst. Electron paramagnetic resonance (EPR) measurements revealed that the incorporation of Rh significantly enhanced the catalyst's ability to adsorb H atoms (Fig. 5e). Furthermore, kinetic isotope effect analysis confirmed that the RhCu NW/CF exhibits faster proton transfer kinetics compared to Cu-based counterparts. Rh facilitates both the generation of *H and its migration to adjacent Cu sites, thereby accelerating the key hydrogenation step of *NO to *NOH, which markedly improves the overall activity and selectivity of the $NO_3RR$ [96].

Furthermore, studies have shown that Mn doping can induce a shift in the adsorption configuration of *NO from a top-site to a bridge-site. This geometric reconfiguration weakens the N–O bond order and lowers the energy barrier for the conversion of *NO to *NOH [97]. Meanwhile, the heteroatomic bonding-induced surface electronic structure reconstruction effectively suppresses the surface oxidation of the Cu catalyst, thereby stabilizing the active sites and enhancing the overall activity and durability of Cu-based catalysts in the $NO_3RR$ [98].

Collectively, these studies demonstrate that bimetallic systems can achieve synergistic enhancement through multidimensional regulation of electronic structures, H transfer, and interfacial configurations. Such cooperative effects offer an effective pathway to

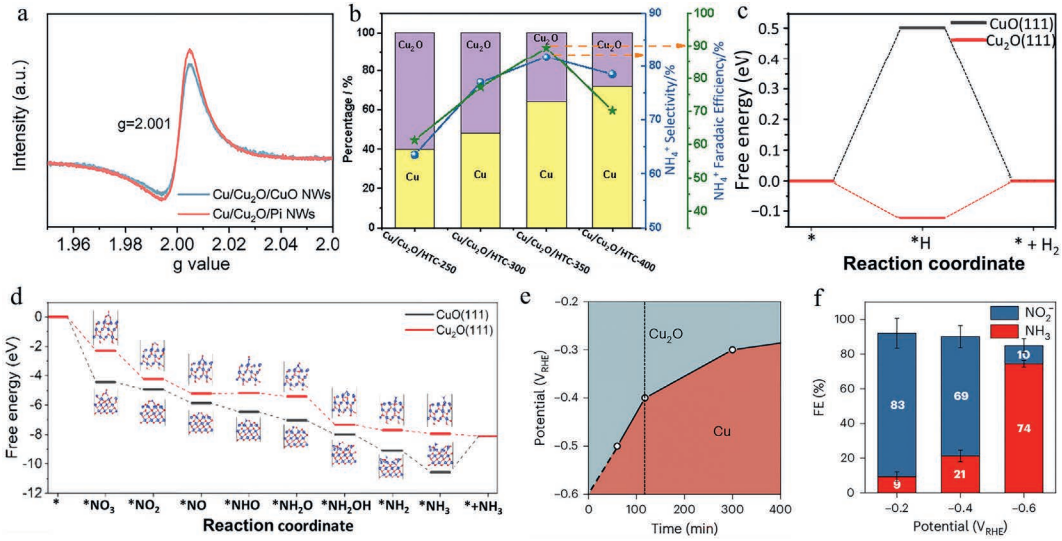



**Fig. 6.** (a) Electron paramagnetic resonance spectra of $Cu/Cu_2O/CuO$ NWs and $Cu/Cu_2O/Pi$ NWs catalysts. Reprinted with permission [101]. Copyright 2024, John Wiley and Sons. (b) Comparison of the performance of catalysts with different Cu and $Cu_2O$ ratios on $NH_4^+$ FE and selectivity at a selected potential. Reprinted with permission [103]. Copyright 2024, Elsevier. (c) Calculated energy distribution of $NO_3RR$ to $NH_3$ on CuO(111) and $Cu_2O(111)$ surfaces. (d) Calculated energy distribution of HER on CuO(111) and $Cu_2O(111)$ surfaces. (c, d) Reprinted with permission [106]. Copyright 2025, Elsevier. (e) The graph illustrates the predominant Cu phase under various potentials and reaction durations. The solid line indicates the time required for a $Cu_2O$ cube to reduce to half its original size. The vertical dashed line denotes the 2 h duration of the $NO_3RR$. The diagonal dashed line extrapolates from 60 min at −0.5 V *vs.* RHE to 0 min at −0.6 V *vs.* RHE. (f) The FE for $NO_2^-$ and $NH_3$ production is presented at potentials of −0.2, −0.4, and −0.6 V *vs.* RHE. (e, f) Reprinted with permission [109]. Copyright 2025, Springer Nature.

overcome the intrinsic limitations of Cu-based catalysts and to develop $NO_3RR$ electrocatalysts with simultaneously high activity, selectivity, and stability.

### 3.4. Oxide-derived Cu catalysts

Cu oxides have been recognized as highly promising candidates for the $NO_3RR$ due to their rich redox properties, tunable valence states ($Cu^0/Cu^+/Cu^{2+}$), and strong interactions with oxygen-containing intermediates. In recent years, oxide-derived Cu catalysts have seen significant advances in $NO_3RR$ applications. Studies have focused on elucidating the intrinsic relationship between their structural features and catalytic activity, while various strategies have been proposed to modulate their electronic structures and surface properties to further enhance reaction performance and selectivity.

Researchers commonly employ metal doping strategies to modify Cu oxides. For instance, studies incorporating transition metals such as Pd and Ni into Cu oxide matrices have demonstrated efficient catalysis driven by synergistic effects between the dopant metals and the Cu oxide substrate. Specifically, the transition metal sites facilitate the generation of *H, accelerating the hydrogenation of $NO_3^-$ reduction. Concurrently, the Cu oxide component governs $NO_3^-$ adsorption and subsequent formation of $NH_3$ [44,99].

For example, Li *et al.* developed a series of Cu-based layered double hydroxides (CuM-LDHs, where M = Ni, Co, Fe, *etc.*) to systematically investigate the effect of heteroatom doping on the concentration and lifetime of surface-active *H. Their study revealed that moderate *H enrichment significantly promotes the hydrogenation of key intermediates such as *NO, thereby enhancing both $NH_3$ selectivity and yield. Specifically, $Cu(OH)_2$ serves as the primary site for $NO_3^-$ adsorption and initial activation, while the incorporated Ni facilitates water dissociation to generate *H and effectively suppresses the competing HER. As a result, CuNi-LDHs exhibited the highest $NO_3RR$ performance among the tested catalysts. This work establishes a clear structure-activity relationship between *H dynamics and $NO_3^-$ reduction efficiency, offering theoretical guidance for the rational design of Cu-based composite catalysts [100].

The regulation of Cu oxidation states is of great significance. Through an electro-driven directed-evolution strategy, the Cu nanowires reconstruct into a $Cu^0$-$Cu^+$ ($Cu_2O$) heterostructure enriched with oxygen vacancies (Fig. 6a), which markedly enhance $NO_x^-$ intermediate adsorption and lower the initial deoxygenation barriers. Subsequent phosphorization forms surface-bound phosphate that stabilize $Cu^+$ and promote H generation, thereby accelerating the deep hydrogenation of $NO_2^-$. Consequently, the hydrogenation capability of $Cu^0$, acts synergistically with the strong $NO_x^-$ affinity of OV-rich $Cu_2O$, delivering a highly efficient and selective $NO_3RR$ [101]. Some studies have specifically demonstrated that the $Cu/Cu_2O$ interface promotes the formation of NOH(ads) intermediates while effectively suppressing $H_2$ evolution [102]. The distribution of the oxidation state of Cu is closely related to $NH_3$ generation. In another study, a series of $Cu/Cu_2O$ materials prepared by thermal decomposition of $Cu(NO_3)_2$ on hydrothermal carbon (HTC) surfaces exhibited enhanced $NO_3^-$ adsorption and hydrogenation capabilities. By tuning the synthesis temperature, the optimal $Cu/Cu_2O$ ratio was achieved, leading to a maximum $NH_3$ FE of 89.5 % and a selectivity of 81.7 % (Fig. 6b) [103].

Modulating the phase transformation behavior of Cu-based catalysts during the reaction has been demonstrated as an effective strategy to enhance the performance. For example, OV-rich spherical CuO NPs undergo *in situ* reconstruction into a $Cu/Cu(OH)_2$ composite structure during $NO_3RR$, forming a layered network that significantly increases the number of exposed active sites. In this system, the metallic Cu component exposes Cu(111) facets, which promote the hydrogenation of key intermediates, while the $Cu(OH)_2$ component presents $Cu(OH)_2(021)$ facets with strong $NO_3^-$ adsorption capability, effectively suppressing the HER. The synergistic interaction at the $Cu/Cu(OH)_2$ interface further facilitates $NO_3^-$ activation and subsequent hydrogenation steps, collectively enhancing $NH_3$ selectivity and reaction rate [104]. A study reported the

synthesis of a $Cu_2O/Cu(OH)_2$ heterojunction, in which $Cu(OH)_2$ extracts electrons from $Cu_2O$, thereby shifting the d-band center of Cu in $Cu_2O$ closer to the Fermi level, which facilitates the adsorption and activation of reaction intermediates [105]. Furthermore, the synergistic effect of Cu(I) and Cu(II) has also been demonstrated in $NO_3RR$. In one study, CuO NPs were supported on nitrogen-doped porous carbon (CuO@NC), and the catalyst was found to form Cu(I)-Cu(II) pairs during the reaction. The redox cycling between Cu(I) and Cu(II) facilitates electron transfer, where Cu(I) significantly reduces the energy barrier for $NO_3RR$ (Fig. 6d), while Cu(II) effectively suppresses the competing HER (Fig. 6c), thereby enhancing the selectivity and efficiency of the $NO_3RR$ process [106].

In existing studies, there is no clear consensus on the optimal Cu oxidation state for reaction process. Some reports highlight the synergistic role of $Cu^+/Cu^{2+}$ redox pairs in enhancing catalytic activity, while others highlight the superior performance of $Cu^+$ and have developed catalyst structures capable of stabilizing this valence state to further improve reaction efficiency. Recent studies show that electron-deficient Cu(I) sites enhance $NH_3$ production in $NO_3RR$ by promoting electron transfer and suppressing the HER [107]. Based on this, Chen *et al.* developed a Ti(III)-modified Ti-$Cu_2O$/Cu catalyst featuring a self-cycling electron donor charge compensation strategy. Ti(III) dynamically reduces Cu to active Cu(I) sites and regenerates itself *via* Ti(III)/Ti(IV) redox cycling. DFT calculations reveal that Ti(III) lowers the Cu positive charge (+0.26 *vs.* +0.34), inhibits over-oxidation, strengthens $NO_3^-$ adsorption (−1.33 eV *vs.* −0.30 eV), and promotes electron transfer (0.69 $e^-$ *vs*. 0.66 $e^-$), enhancing $NO_3^-$ activation. At −0.9 V *vs.* RHE, the catalyst achieves 95.0 % $NO_3^-$ removal, 95.5 % $NH_3$ selectivity, and excellent stability, offering a promising strategy for efficient $NO_3RR$ catalyst design [108].

Cu oxides, due to their variable oxidation states and rich surface structures, are prone to phase transformations during electrocatalytic reactions. Studies have shown that the reduction of Cu oxides to metallic $Cu^0$ during the $NO_3RR$ can significantly enhance $NH_3$ production performance. Recently, Yoon *et al.* employed *operando* electron microscopy combined with multimodal spectroscopic techniques to systematically reveal the potential- and time-dependent structural evolution of $Cu_2O$ precatalysts under $NO_3RR$ conditions. The study found that under moderately reductive potentials, $Cu_2O$ and metallic Cu can coexist in a spatially separated manner, with their relative proportions being regulated by the electrolyte composition and the applied potential. As the potential becomes more negative, the reduction of $Cu_2O$ accelerates, leading to an increased fraction of $Cu^0$ and a corresponding enhancement in the FE of $NH_3$ (Figs. 6e and f). Moreover, the study pointed out that under conditions of elevated local pH, a passivating layer of $Cu(OH)_2$ tends to form on the catalyst surface, hindering the direct contact of electrons and protons with the underlying $Cu_2O$. This delays its reduction to metallic Cu, thereby affecting the overall phase transition kinetics and the final product selectivity of the catalyst [109]. The work demonstrates that the dynamic phase transition from $Cu_2O$ to $Cu^0$ plays a decisive role in determining the catalytic performance of $NO_3RR$, highlighting the critical importance of phase transformation behavior in tuning reaction activity and selectivity.

Regulating the oxidation state of Cu aims to achieve optimal synergy between $NO_3^-$ activation and the hydrogenation step, thereby enabling precise control over product selectivity. Given that Cu species with different valence states exhibit markedly different catalytic behaviors under varying reaction environments (*e.g.*, pH, potential, and electrolyte composition), the rational design of catalysts capable of stabilizing specific advantageous oxidation states is crucial for achieving both high activity and long-term stability in $NO_3RR$.

### 3.5. Cu single-atom catalysts (SACs)

SACs are structurally distinct from traditional nanoparticle catalysts, with metal active components anchored on the carrier surface in the form of isolated atoms, achieving the characteristic of full exposure of metal atoms. This atomically dispersed structure not only endows the catalyst with fully exposed low-coordinated metal active centers but also effectively promotes the adsorption and activation of reactants and the interfacial mass transfer process [110]. Meanwhile, the strong coordination between single atoms and their surrounding ligands provides robust structural support for metal centers, significantly enhancing the structural stability of the catalyst [111].

Recently, Shan *et al.* incorporated single atoms of Mn, Fe, Co, Ni, and Cu into the defect sites of UiO-66 to construct a series of MOF-derived single-atom catalysts (M-SACs), among which Cu-SAC and Fe-SAC exhibited the most outstanding electrocatalytic performance. Characterizations confirm that Cu-SAC exhibits excellent atomic dispersion, with the single-atom structure remaining well-preserved after 16 h of continuous operation. DFT calculations revealed that Cu-SAC has lower reaction energy barriers for $^*NO_3$ adsorption and subsequent hydrogenation steps, which explains its high catalytic performance [112]. These results clearly demonstrate the superior performance and application potential of Cu SACs compared to other metal candidates.

Cu SACs typically utilize carbon-based supports due to their high specific surface area and excellent electrical conductivity. Chen *et al.* developed a novel Cu SAC, Cu-N-C, which produced more $NH_3$ (Fig. 7a) and less $NO_2^-$ (Fig. 7b) compared to pure Cu and other control samples. This enhanced selectivity originates from isolated Cu-$N_4$ single-atom sites that thermodynamically inhibit N–N coupling, thereby suppressing the formation of dinitrogen byproducts. DFT calculations and *in-situ* DEMS respectively confirmed that the single-atom site nature lowers the potential-limiting step barrier to only 0.09 eV and that the formation of $N_2/N_2O$ is negligible [113]. Furthermore, Zhu *et al.* controlled the aggregation state of Cu atoms by varying the annealing temperature; with increasing temperature, the isolated Cu atoms gradually aggregated into NPs or clusters. Among the catalysts, Cu-N-C-800 featured uniformly dispersed Cu atoms anchored on nitrogen-doped carbon nanosheets, exhibiting superior electrocatalytic performance compared to Cu NPs and Cu plate-800 (Fig. 7c), while effectively suppressing the formation of $NO_2^-$ (Fig. 7d). DFT calculations demonstrated that the strong adsorption of $NO_3^-$ and $NO_2^-$ on single-atom Cu-$N_x$ sites facilitate the reaction and suppress $NO_2^-$ release [114].

In addition, the synthesis of bimetallic single-atom catalysts (BSACs) is an effective strategy for enhancing performance. The synergistic action of two metal single atoms enhances $NH_3$ production. For example, the Fe/Cu dual-atom catalyst (Fe/Cu-HNG) reported on porous N-doped graphene reduced the adsorption barrier of $NO_3^-$, making the NO molecule easier to activate and promoting the hydrogenation step, thereby significantly improving the catalytic activity of $NO_3RR$ from $NO_3^-$ to $NH_3$ [115]. Several studies have dispersed foreign metal atoms (*e.g.*, Ni, Pd, Au) on the surface of Cu substrate for catalytic applications [116–118]. Yu *et al.* synthesized Au-Cu single-atom alloy aerogels ($Au_mCu$ SAAs) that demonstrate >90 % FE across 0 to −1 V *vs.* RHE, and exhibit near 100 % $NH_3$ FE with 6.21 mmol $h^{-1}$ $cm^{-2}$ production rate at −0.8 V *vs.* RHE. Au site lowers the $^*NO_2$ to $^*NOOH$ hydrogenation barrier and precisely dissociates $H_2O$ to supply $^*H$ on demand; its down-shifted d-band center weakens $^*H$ adsorption to suppress HER, while simultaneously upshifting the d-band of adjacent Cu sites to strengthen $NO_3^-/^*NO_2$ adsorption [119]. Novel concepts for $NO_3RR$ catalyst design are generated by the synergistic impact of dual atoms.

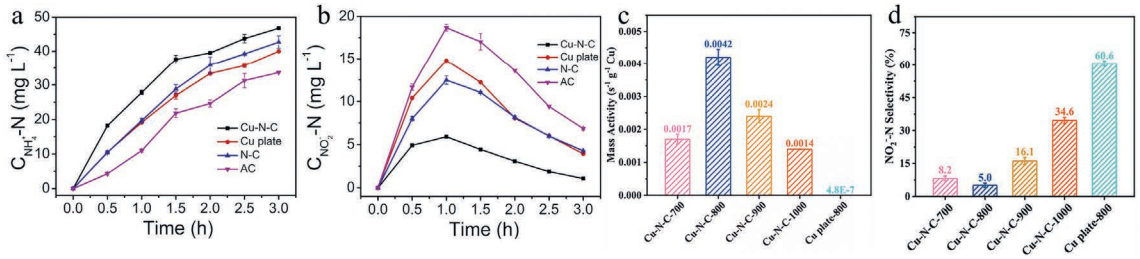



**Fig. 7.** (a) The comparison of the selectivity of $NO_3RR$ to $NH_4^+$ under different catalysts at the selected voltage and (b) comparison of $NO_2^-$ concentration in $NO_3RR$ over different catalysts at selected voltage. (a, b) Reprinted with permission [113]. Copyright 2022, Elsevier. (c) Comparison of mass activity of different cathode materials and (d) comparison of $NO_2^-$-N selectivity of different cathode materials. (c, d) Reprinted with permission [114]. Copyright 2020, John Wiley and Sons.

To evaluate several Cu-based catalysts' catalytic activity in the $NO_3RR$ in more detail, we have systematically compiled representative catalysts from previous studies along with their key parameters, such as material type, electrolyte environment, operating potential, $NH_3$ selectivity, and yield, as summarized in Table S1 (Supporting information).

Cu-based catalysts have demonstrated certain catalytic activity in $NO_3RR$, but they still face several limitations that hinder their practical applications. Firstly, Cu-based catalysts are prone to deactivation during the reaction, as their surface often undergoes morphological and chemical state reconstruction under electrochemical conditions, leading to unstable catalytic performance [120–122]. Secondly, the intermediate or by-product species generated during the reaction tend to strongly adsorb on the catalyst surface, blocking active sites, reducing catalytic efficiency, and significantly decreasing activity [123,124]. Some modification methods involve complex structural regulation, making large-scale preparation difficult and are prone to HER under high current densities. These drawbacks limit the practical deployment of Cu-based catalysts, necessitating optimization through material design and surface engineering. In the future, it will be important to explore new regulation strategies to achieve precise control over the structure and interfacial microenvironment of Cu-based catalysts, further enhancing their activity, selectivity, and stability in $NO_3RR$ and laying the foundation for their practical application in environmental remediation and resource utilization.

## 4. Electrolyte influence

Electrolytes are critical in $NO_3RR$ for $NH_3$ synthesis, providing the environment for interactions between $NO_3^-$ and catalysts and serving as the medium for the reduction process. To enhance electrocatalytic performance, while developing efficient electrocatalysts is crucial, regulating the electrolyte's microenvironment has become an equally important strategy. This microenvironment, influenced by factors such as electrolyte concentration, local pH, and cation and anion effects, significantly impacts the $NO_3^-$ reduction process [125,126].

Regulating proton supply and modifying electrode surface characteristics are the primary means by which the pH of the electrolyte influences the $NO_3RR$ to $NH_3$. Yan *et al.* investigated the activity and selectivity of Fe, Co, Ni, and Mn SACs supported on the same substrate under various pH conditions. The study revealed that the paths of reactions, potential-determining steps, and limiting potentials of these metal catalysts in $NO_3RR$ exhibit pH-dependent characteristics. Taking the EA-Co catalyst as an example, Figs. S2a-c (Supporting information) clearly illustrate the variations in catalytic performance under different pH conditions. Under acidic conditions (pH 0), the electrolyte presents a high chemical potential of protons, so the late-stage hydrogenation sequence operates along a markedly exothermic profile. The potential determining step (PDS) corresponds to the conversion of $NH^*$ to $NH_2^*$, with a limiting potential of −0.37 V *vs.* RHE, indicating high catalytic activity. When the environment shifts to neutral conditions (pH 7), the proton reservoir is largely sustained by water autoionization; the consequent scarcity of $H^+$ markedly attenuates the driving force for the hydrogenation sequence. Although the PDS remains unchanged, its free-energy ascent turns endergonic, pushing the limiting potential to +0.40 V *vs.* RHE and causing a pronounced drop in catalytic throughput. Under alkaline conditions (pH 14), the virtual absence of bulk protons forces the interface to rely on water dissociation as the dominant hydrogen supplier; this shift reorders the relative stabilities of key intermediates, advancing the PDS to the $NO^*$ to $NOH_2^*$, and steering the reaction into a distinct pathway governed by a markedly different kinetic regime [127]. Generally, most catalysts exhibit superior performance in alkaline environments [128–130]. Wu *et al.* tested the Fe SAC in electrolytes with pH values of 1 and 13, and the results showed that the catalyst achieved higher $NH_3$ FE in the alkaline environment [131]. In neutral environments, numerous studies have also enhanced performance by increasing local pH, promoting water dissociation, and inhibiting the combination of $^*H$ [130,132,133]. For Cu catalysts, there is a type of catalyst where Cu was encapsulated within hydrophilic hierarchical nitrogen-doped carbon nanocages (Cu@hNCNC). In this structure, the hNCNC shell effectively restricted the diffusion of generated $OH^-$, leading to an elevated pH microenvironment surrounding the Cu NPs inside. The locally generated alkaline microenvironment within neutral electrolyte effectively suppressed parasitic HER, enabling efficient $NO_3^-/NO_2^-$ to $NH_3$ conversion with 99.7 % FE and a record-high production rate of 4.0 mol $h^{-1}$ $g^{-1}$ [134]. In acidic electrolytes, protons originate from $H^+$, and the abundance of $H^+$ can promote the reaction of $NO_3^-$ to $NH_3$. However, excessively low pH values may corrode electrode materials or trigger oxygen evolution reaction side reactions, affecting the stability and lifespan of the electrode. Chen *et al.* proposed a conductive polymer protection strategy by decorating polypyrrole (PPy) on Cu NPs, enabling efficient $NO_3RR$ to $NH_3$ under highly acidic conditions. Even in a highly acidic electrolyte containing 0.5 mol/L $H_2SO_4$, the catalyst demonstrated outstanding performance, with an $NH_3$ yield rate of 0.55 mmol $h^{-1}$ $cm^{-2}$, a selectivity of 99.99 %, and a FE of 96.0 %. PPy enhanced the catalyst performance through multiple mechanisms, including protecting Cu NPs from corrosion, enhancing the adsorption capacity of $NO_3^-$ and $NO_2^-$ at the interface, stabilizing the intermediate valence states of Cu active centers, and establishing efficient electron transport pathways, thereby facilitating efficient $NH_3$ generation [135]. At the same time, in acidic media, HER inevitably becomes a competitive reaction of $NO_3RR$ [136]. Most of the reported $NO_3RR$ catalysts suitable for alkaline environments are unstable under acidic conditions [137]. These electrocatalysts may undergo significant HER in acidic media, resulting in a decrease in the selectivity of the target product. $TiO_2$ has HER inertness and significant corrosion resistance [138]. In a study, the properties of $TiO_2$ under acidic, neutral and alkaline conditions were tested: Under

acidic conditions, $TiO_2$ showed a more positive starting point and a higher current density (Figs. S2d and e in Supporting information), and the FE of $NO_3^-$ reduction to $NH_3$ was the highest, up to 82 %. The main reason is that high concentration of $H^+$ and $NO_3^-$ help to improve selectivity and inhibit side reactions. As an electrode material, Ti has good corrosion resistance and can be stable in a strong acidic environment. The yield of $NH_3$ under neutral and alkaline conditions was relatively low, which was mainly affected by the insufficient concentration of $H^+$ or excessive $OH^-$, resulting in the competitive reduction of $NO_3$RR and the formation of by-products [139].

The performance of different catalysts varies significantly under different pH conditions, highlighting the critical importance of selecting an appropriate pH environment to optimize catalytic performance. For instance, $TiO_2$ nanosheets with weak hydrogen activity can effectively suppress the HER in acidic electrolytes, thereby achieving high-selectivity to $NH_3$ [139]. By contrast, Ni exhibits the opposite trend, displaying higher hydrogen evolution activity under alkaline conditions than in acidic media [140]. This further underscores that both the intrinsic hydrogen-evolution capability of the catalyst and the appropriate matching of pH must be considered simultaneously. Through structural modifications, such as the use of Fe-Ni tandem catalysis, enhanced performance can be achieved in alkaline environments [141]. Additionally, CuNi alloys have demonstrated excellent catalytic performance in neutral conditions [142]. These studies indicate that the hydrogen evolution capability of a catalyst, as well as its structural design, are key factors influencing catalytic performance, and the judicious selection of pH environment can further optimize the performance of the catalyst.

In addition to pH, $NO_3^-$ concentration significantly influences the performance of $NO_3$RR to $NH_3$. Typically, most $NO_3$RR studies are conducted under low reactant concentrations (<1 mol/L), and the reduction process generally follows the Langmuir-Hinshelwood kinetic model, exhibiting concentration-dependent shifts in reaction order. Specifically, in different catalyst systems, as the $NO_3^-$ concentration increases and the surface active sites approach saturation, the reaction rate may gradually shift from first-order to zero-order kinetics. The concentration threshold at which this transition occurs varies depending on the type of catalyst and the reaction conditions [126,143,144]. Under $NO_3^-$-deficient conditions, the mass transfer is limited and the $NO_3^-$ diffusion efficiency is low, which leads to the intensification of HER competition and limits the reactants to reach the active site. The performance increases with the rise in $NO_3$–N concentration until the active sites become saturated with adsorbed species [126]. On the contrary, at higher concentrations, the catalyst surface is covered by excessive $^*NO_x$ species. This coverage not only restricts the accessibility of active sites but also decelerates the processes of electron transfer and transformation of reaction intermediates, thereby affecting subsequent hydrogenation steps and ultimately leading to the accumulation of $NO_2^-$ intermediates on the catalyst surface [145]. For example, as the concentration of the diluted $NO_3^-$ increased from 0.01 mol/L to 0.1 mol/L, the enhanced mass transfer led to an increase in the $NH_3$ production rate of the $Cu_2O$ catalyst. The competitive adsorption between water molecules and $NO_3^-$ at elevated concentrations (0.1–3 mol/L) induced a 32 % decline in $Cu_2O$ catalytic performance, attributed to active site saturation under $NO_3^-$-dominated reaction conditions. Hu *et al.* adjusted the kinetic curve by introducing Ru on the surface of $Cu_2O$. Ru/$Cu_2O$ can significantly increase the $NH_3$ production rate by 13 times when the $NO_3^-$ concentration increases from 0.01 mol/L to 1 mol/L, and also has considerable performance at 3 mol/L (Fig. S2f in Supporting information) [146]. Increasing $NO_3^-$ concentration can enhance $NH_3$ yield in $NO_3$RR by improving mass transfer, but excessive concentrations may lead to active site saturation and hinder catalytic performance. Therefore, optimizing the $NO_3^-$ concentration is crucial for balancing activity and selectivity in $NO_3$RR systems.

The cations and anions in the electrolyte also significantly influence the $NO_3^-$ reduction rate. Some anions can form competitive adsorption with $NO_3^-$, reducing the adsorption efficiency of $NO_3^-$ and slowing down the removal rate [147]. At the corresponding operating voltage, the influence of anions on the $NO_3^-$ reduction rate was found to follow the order: $I^- > Br^- > Cl^- > F^-$ (Fig. S2g in Supporting information) [148], with larger radius halide anions having a smaller inhibitory effect on the reaction rate. Furthermore, the anode may oxidize a significant amount of $Cl^-$ in industrial effluent to $Cl_2$, and $Cl_2$ can hydrolyze to form $ClO^-$, which can readily oxidize $NH_3$ to $N_2$. The introduction of $Cl^-$ into the electrolyte can increase the selectivity for $N_2$. Studies have demonstrated that increasing the $Cl^-$ concentration from 0.01 mol/L to 0.04 mol/L facilitates the anodic electro-chlorination to generate active chlorine species ($Cl_2$/HClO/$ClO^-$), which subsequently promotes the further oxidation of $NH_4^+$ to $N_2$, thereby boosting the nitrogen selectivity from approximately 45 % to 98 % [149]. Guo and associates also investigated the impact of oxalate ions on catalytic performance. They found that in acidic and alkaline electrolytes, a substantial fraction of Cu sites on the Cu foil surface were occupied by oxalate ions, forming competitive adsorption with $NO_3^-$ and thus inhibiting the catalytic activity of the Cu foil. However, this inhibitory effect of oxalate ions was not observed in neutral electrolytes [150]. Similarly, $SO_4^{2-}$ and $ClO_4^-$ also exert an inhibitory effect on $NO_3^-$ adsorption [144].

Cations modulate the rate and selectivity of the $NO_3$RR process by adjusting the catalyst's electronic configuration, impacting $NO_3^-$ adsorption, modifying intermediate stability, and restructuring the electrical double layer (EDL). In this process, the impact of different alkali metal cations on the proton transfer rate within the EDL is particularly significant. Wen *et al.* used elemental Cu as a model electrocatalyst and found that the order of catalytic activity, FE, and selectivity for $NH_3$ synthesis in electrolytes containing different cations was $Li^+ < Cs^+ < Na^+ < K^+$ (Fig. S2h in Supporting information). Theoretical calculations reveal that the presence of $K^+$ induces a more negative shift in the electrostatic potential within the EDL, thereby reducing the energy barrier for protons to cross the EDL and reach the catalyst surface, thus accelerating proton transfer. Moreover, $K^+$ facilitates the coupling of protons with $NO_3^-$-containing intermediates, enabling a more efficient reduction of $NO_3^-$ to $NH_3$. The experimental results further validate the superior performance of $K^+$ in enhancing the $NO_3$RR, especially in terms of improving $NH_3$ generation efficiency and reducing reaction energy barriers [151]. Duarte *et al.* conducted experiments using a Ni cathode in electrolytes containing hexavalent chromium, and when hexavalent chromium was reduced to trivalent chromium, a layer of hydroxide chromium emerged on the cathode surface, functioning as an insulating barrier that impeded the migration of reduction electrons [152]. Furthermore, the adsorption of $Ca^{2+}$ and $Mg^{2+}$ on the cathode surface leads to the formation of precipitates, which subsequently poison the active sites and inhibit $NO_3$RR [153]. Unlike reversible competitive adsorption by anions, such precipitate coverage represents irreversible surface passivation, which not only physically masks catalytic sites but also significantly enhances interfacial mass-transfer resistance, thereby diminishing the catalytic activity for $NO_3^-$ reduction. Therefore, in the $NO_3$RR, the roles of anions and cations in the electrolyte must not be overlooked, and optimizing their regulatory mechanisms is key to improving the reaction performance.

Precise regulation of electrolyte parameters plays a crucial role in optimizing electrochemical reaction conditions, thereby enhancing reaction efficiency and product selectivity during $NO_3$RR for $NH_3$ synthesis. Adjusting the pH of the electrolyte can significantly influence the reaction rate and pathways, while tuning the salt

concentration facilitates mass transfer. Additionally, the rational selection of cations and anions helps stabilize reaction intermediates and promotes the formation of target products. Therefore, precise control of the electrolyte composition represents an important strategy for achieving efficient, energy-saving, and highly selective electrochemical synthesis.

## 5. Conclusion and perspectives

### 5.1. Conclusion

The $NO_3$RR is a significant electrocatalytic process with broad application prospects in various fields. It not only serves as an effective method for removing $NO_3^-$ pollution from wastewater but also selectively converts $NO_3^-$ into valuable nitrogen-containing compounds. This review summarizes the reaction pathways of $NO_3^-$ reduction, outlines methods for detecting products and intermediates, and highlights the recent advancements in Cu-based catalysts for $NO_3$RR, covering different material design strategies such as nanostructure control, specific crystal face exposure, alloying modification, oxidation state regulation, and the application of single-atom catalysis. These strategies influence the electronic structure and distribution of active sites of the catalysts, and to some extent, determine the reaction pathways and selectivity of the target products. Each type of catalyst has its own advantages and disadvantages. For example, single-metal Cu catalysts have a simple composition and a single type of active site, which facilitates the study of structure-activity relationships. However, pure Cu catalysts mainly produce $NO_2^-$ in the reaction, and the hydrogenation reaction is limited. Composite catalysts boost $NH_3$ synthesis efficiency by precisely regulating the adsorption-desorption kinetics of intermediates and reducing energy barriers in proton-coupled electron transfer pathways. However, issues such as catalyst passivation may arise during the catalytic process. Additionally, we explored the effect of the electrolyte environment on the catalytic performance of $NO_3$RR, including changes in pH value, the role of different cations and anions, and the regulation of $NO_3^-$ concentration on reaction kinetics, providing theoretical guidance for optimizing electrolyte conditions and improving catalytic efficiency.

### 5.2. Perspectives

The electrocatalytically-driven conversion of $NO_3^-$ to $NH_3$ enables sustainable nitrogen cycle remediation, offering multifunctional potential in advanced wastewater treatment, electrochemical energy reservoirs, and carbon-neutral chemical synthesis systems. However, this process involves multiple electron-proton transfers and is highly dependent on the catalyst. Current Cu-based catalysts are constrained by insufficient catalytic efficiency, inadequate durability, and dominant competition from the HER. To enable industrial implementation, future investigations must not only overcome these inherent limitations but also systematically focus on and address the following critical aspects:

(1) Prospects for multidimensional regulation strategies of Cu-based $NO_3$RR *catalysts*

To further enhance the activity and selectivity of Cu-based catalysts in the $NO_3$RR, interface microenvironment engineering holds significant promise. Organic molecule modification has emerged as an effective strategy. By introducing functional groups such as amines, imidazoles, or polyelectrolytes, the surface electronic structure of the catalyst and the adsorption behavior of key intermediates can be precisely modulated. For instance, a positively charged polyethyleneimine layer can create a favorable interfacial environment by enriching $NO_3^-$, weakening the interaction between *NO and Cu active sites, and accelerating *NO hydrogenation, resulting in a FE for $NH_3$ exceeding 90% [154]. Furthermore, Qin *et al.* developed a strategy to effectively "capture" $NO_3^-$ by modifying Co oxide with a protic ionic liquid to modulate the electrode surface microenvironment, mimicking the environment of the MoFe protein in nitrogenase. This approach successfully enhanced both the $NH_3$ yield and FE in the $NO_3$RR process [155]. Interfacial wettability regulation, a relatively novel yet highly promising strategy, has shown efficacy in electrochemical systems such as carbon dioxide reduction reaction and oxygen evolution reaction [156,157]. Future efforts could focus on constructing spatially heterogeneous wettability interfaces on Cu-based electrodes, such as alternating hydrophilic/hydrophobic domains or charged organic layers. These designs may enable the local enrichment of $NO_3^-$, suppress competing HER, and further enhance $NH_3$ selectivity.

In addition to catalyst-centric design, regulation of the reaction environment is also critical to performance optimization. External-field-assisted modulation (*e.g.*, electric, magnetic, photonic, and thermal fields) enhances performance [158]. Applied electric or magnetic fields can steer the transfer pathways of electrons and protons, promoting N–H bond formation while suppressing undesired N–N coupling. Meanwhile, the synergistic effects of photothermal energy and photogenerated charge carriers can influence the adsorption and transformation kinetics of key intermediates such as *NO. Integrating these fields with catalyst and interface design overcomes kinetic limitations and boosts activity and selectivity.

(2) Focus on products other than $NH_3$

Electrochemical reduction reactions often occur under complex interfacial conditions, and in addition to $NH_3$, other products may be generated. During the reduction process, $NO_3^-$ may first be reduced to $NO_2^-$, which can accumulate if the reduction is incomplete. $NO_2^-$ is an unstable compound that can further react to form products such as $N_2$, NO, and $N_2O$. Additionally, other possible products include nitrous acid ($HNO_2$), NO, $NO_2$, $N_2$, and $H_2$. The generation of by-products can reduce the efficiency of the main product. In the study and optimization of electrocatalytic $NO_3^-$ reduction, it is necessary to systematically monitor the formation of these by-products. Gaining insights into products beyond $NH_3$ can offer a holistic comprehension of the reaction mechanism and efficacy. By studying the generation and quantity changes of by-products, the selectivity and efficiency of the reaction can be assessed, and reaction conditions and catalyst designs can be further optimized.

(3) The potential of AI in catalyst design for $NO_3$RR

Currently, research in this field primarily relies on traditional trial-and-error experiments combined with DFT calculations. However, these approaches exhibit low efficiency in screening high-performance catalysts and optimizing reaction parameters, making it difficult to comprehensively explore the complex parameter space [159]. Recently, AI techniques have demonstrated the potential to accelerate catalyst development and mechanistic insights in areas such as $CO_2$RR and HER [160,161]. For example, Xu *et al.* employed AI-driven methods using a training set of 736 catalysts, combined with feature compression and subgroup discovery, to extract key descriptors (*e.g.*, d-band center and formation energy), which increased the screening accuracy for high-performance single-atom catalysts for ORR from 14% to 60%. They further conducted high-throughput predictions across 10,179 candidate systems and experimentally validated the identified optimal catalysts [162]. Moreover, studies have combined the PaiNN model with multi-task genetic algorithms to achieve high-throughput

screening and optimization of catalyst surface structures [163]. In the investigation of catalytic mechanisms, researchers have integrated experimental characterization techniques such as powder X-ray diffraction (PXRD), Raman spectroscopy, and *in situ* X-ray absorption spectroscopy (XAS) with AI-driven approaches like artificial neural networks (ANN) and Monte Carlo simulations. This multifaceted strategy has been employed to thoroughly explore the active sites and surface reconstruction mechanisms of $CuO/CeO_2$ catalysts, thereby enhancing research efficiency and providing a more comprehensive understanding of the intricate catalytic processes [164]. Leveraging machine-learning potentials (MLPs) enables the simulation of atomic behavior at complex interfaces and during dynamic processes, thereby providing a clear elucidation of reaction pathways and the stability of intermediates [165].

Currently, the application of AI in $NO_3RR$ is still in its infancy, but the introduction of advanced computational methods holds promise for accelerating the development of catalysts, enabling efficient screening, predicting reaction pathways and the stability of intermediates, and gaining in-depth insights into how the composition of the electrolyte and the applied potential influence performance. When combined with *in situ* characterization techniques, these methods can rapidly identify and accurately attribute intermediates, thereby enhancing the precision of predictions and laying a solid foundation for mechanistic studies and large-scale applications. Looking ahead, the development of Interpretable data models and their integration with automated experimental platforms to create a closed-loop process from screening to validation will facilitate the rapid advancement and practical implementation of efficient catalysts and $NO_3RR$ systems.

(4) The development of co-electrolysis systems to produce high-value products

How to efficiently utilize $NO_3^-$ and convert it into more valuable chemicals should be a topic of concern. Currently, there are studies that have achieved the co-electrolytic synthesis of high-value products by reducing $NO_3^-$ with other substances. For example, an electrochemical synthesis of essential $NH_3$-based amino acids driven by NO and $\alpha$-keto acids has been reported, and this strategy is also applicable to the synthesis of other $NH_3$-based amino acids from $NO_3^-$ [166]. By integrating $CO_2$ and $NO_3^-$ electrolysis into a unified urea synthesis process, this strategy not only mitigates greenhouse gas emissions but also transforms $NO_3^-$ pollutants from industrial effluents into valuable feedstocks, thereby facilitating the advancement of sustainable resource management. Studies have shown that vitamin $B_{12}$ immobilized on carbon nanotube surfaces can catalyze the co-electrolytic synthesis of urea [167], and carbon nanotube-supported cobalt $\beta$-amino acid eye alkaloid molecular catalysts can electrocatalytically convert $CO_2$ and $NO_3^-$ into methylamine [168]. $NH_3$-based amino acids, urea, and amines are exemplars of high-value products with extensive applications across diverse industrial sectors and a demand that is progressively increasing. $NO_3^-$ is one of the common water pollutants. The advancement of electrochemical co-electrolysis systems targeting $NO_3^-$ not only mitigates emissions and conserves energy but also facilitates waste management and environmental protection. Moreover, it plays a vital role in stimulating economic development.

(5) Critical challenges of Cu-Based catalysts in industrial applications and advances in electrolyzer systems and catalyst film technologies

Despite the promising $NO_3^-$ reduction activity and product selectivity exhibited by Cu-based catalysts under idealized laboratory conditions, their practical application in complex industrial wastewater systems still faces multiple critical challenges.

First, $NO_3^-$ concentrations in industrial effluents vary widely. These effluents are often accompanied by a multitude of inorganic ions (*e.g.*, $Cl^-$, $SO_4^{2-}$) and organic contaminants. These coexisting species can block active sites or compete for electrons, markedly lowering both activity and $NH_3$ selectivity. Second, environmental parameters such as pH, conductivity, and dissolved oxygen in real wastewater fluctuate dynamically. These conditions can intensify competing side reactions like the HER, ultimately decreasing the FE for $NH_3$ production. Moreover, Cu-based materials exhibit limited chemical stability in strongly acidic or alkaline media, where corrosion or surface restructuring may occur, leading to catalyst deactivation over time. For example, a polymer-molecule electrode loaded with Cu (ME-Cu), developed by Su *et al.*, demonstrated stable $NO_3RR$ operation for approximately 100 h [169]. However, this operational lifetime is far from sufficient when compared with commercial systems, such as the 2.5 kW anion exchange membrane electrolyzer from Stable Stone Hydrogen Energy, which can stably operate for over 1000 h. Third, most current studies rely on simplified, high-purity electrolyte systems, lacking long-term electrolysis validation under more realistic conditions. This is especially true at low ($<$50 mg/L) or high ($>$1000 mg/L) $NO_3^-$ concentrations. This limits the translatability of lab-scale results to real-world applications. In real-world scenarios, $NO_3^-$ concentrations in wastewater are typically low, which poses challenges for efficient mass transfer of $NO_3^-$. To enhance the mass transfer of $NO_3^-$, pre-treatment technologies such as electrodialysis, ion exchange resins, and reverse osmosis are often required to concentrate the $NO_3^-$ in wastewater. However, these additional treatment steps not only increase the complexity of the process but also potentially lead to higher costs. Moreover, the underreporting of key engineering parameters, such as energy consumption, $NH_3$ production FE, and specific energy consumption, hinders a comprehensive assessment of the economic feasibility of the process. To facilitate the transition of $NO_3^-$ reduction technology from the laboratory to industrial applications, future research needs to focus more on optimizing and reporting these critical parameters, as well as conducting long-term electrolysis experiments under conditions that more closely resemble actual engineering scenarios, to ensure that research outcomes can truly meet practical engineering demands.

In addition, the design of the electrochemical reactor represents another major bottleneck toward scale-up. Conventional H-type cells or simplified three-electrode systems are inadequate to replicate industrial fluid dynamics, resistance distribution, or mass transport behaviors. Future efforts should focus on developing advanced modular electrolyzer systems capable of stable operation at high current densities ($>$1 A/cm$^2$), incorporating large-area electrodes ($>$100 cm$^2$) with optimized electric field distribution and efficient reactant/product transport. Integration of key engineering components, such as gas-liquid separation, ion-selective membranes, electrolyte recirculation, and energy recovery units, will be crucial to achieving system-level energy efficiency.

In summary, advancing Cu-based $NO_3RR$ catalysts toward practical industrial deployment requires a synergistic approach that enhances catalyst chemical and structural stability, improves interference resistance under complex aqueous environments, and simultaneously optimizes the design of scalable electrolyzer architectures and film deposition technologies.

## Declaration of competing interest

The authors declare that they have no known competing financial interests or personal relationships that could have appeared to influence the work reported in this paper.

## CRediT authorship contribution statement

**Lewa Zhang:** Writing – review & editing, Writing – original draft, Data curation. **Quan Zhou:** Writing – original draft. **Chenyuan Zhu:** Writing – review & editing, Writing – original draft, Supervision, Conceptualization. **Yizhao Li:** Writing – review & editing, Writing – original draft. **Shihan Zhang:** Supervision, Resources, Conceptualization. **Fan Dong:** Supervision, Resources, Data curation, Conceptualization.

## Acknowledgment

This work was financially supported by the Key R&D Program of Zhejiang (No. 2024C03136).

## Supplementary materials

Supplementary material associated with this article can be found, in the online version, at doi:10.1016/j.cclet.2025.112325.

## References

[1] Y. Ashida, K. Arashiba, K. Nakajima, Y. Nishibayashi, Nature 568 (2019) 536–540.
[2] R.F. Service, Science 345 (2014) 610.
[3] J. Lim, C.A. Fernández, S.W. Lee, M.C. Hatzell, ACS Energy Lett. 6 (2021) 3676–3685.
[4] H. Zhang, K. Fang, J. Yang, et al., Coord. Chem. Rev. 506 (2024) 215723.
[5] X. Liu, P. Liao, W. Liao, S. Wang, G. Li, EnergyChem 7 (2025) 100146.
[6] J. Liu, Z. Li, C. Lv, et al., Mater. Today 73 (2024) 208–259.
[7] C. Smith, A.K. Hill, L. Torrente-Murciano, Energy Environ. Sci. 13 (2020) 331–344.
[8] M. Capdevila-Cortada, Nat. Catal. 2 (2019) 1055 -1055.
[9] S. Ye, Z. Chen, G. Zhang, et al., Energy Environ. Sci. 15 (2022) 760–770.
[10] L. Wang, M. Xia, H. Wang, et al., Joule 2 (2018) 1055–1074.
[11] X. Zhao, G. Hu, G.-F. Chen, et al., Adv. Mater. 33 (2021) 2007650.
[12] A.P. Varghese, S.K. Lakhera, Renew Sustain Energy Rev 200 (2024) 114537.
[13] M. Chen, X. Li, N. Liu, et al., Chin. Chem. Lett. 36 (2025) 111294.
[14] C.C. Lee, W. Kang, A.J. Jasniewski, et al., Nat. Catal. 5 (2022) 443–454.
[15] J. Wang, L. Yu, L. Hu, et al., Nat. Commun. 9 (2018) 1795.
[16] A.C. Nielander, J.M. McEnaney, J.A. Schwalbe, et al., ACS Catal. 9 (2019) 5797–5802.
[17] J.G. Chen, R.M. Crooks, L.C. Seefeldt, et al., Science 360 (2018).
[18] H. Liu, X. Lang, C. Zhu, et al., Angew. Chem. Int. Ed. 61 (2022) e202202556.
[19] Y. Wang, C. Wang, M. Li, Y. Yu, B. Zhang, Chem. Soc. Rev. 50 (2021) 6720–6733.
[20] Z. Li, J. Luo, L. Yao, et al., Chin. Chem. Lett. 37 (2026) 112141.
[21] S. Niu, J. Yang, L. Qian, et al., ChemElectroChem 10 (2023) e202300419.
[22] Y. Zhao, J. Shen, J. Yuan, et al., Nano Energy 124 (2024) 109499.
[23] Q. Liu, G. Wen, D. Zhao, et al., J. Colloid Interface Sci. 623 (2022) 513–519.
[24] J. Qin, K. Wu, L. Chen, et al., J. Mater. Chem. A 10 (2022) 3963–3969.
[25] W. Zhong, Q.L. Hong, X. Ai, et al., Adv. Mater. 36 (2024) 2314351.
[26] Y. Han, X. Zhang, W. Cai, et al., J. Colloid Interface Sci. 600 (2021) 620–628.
[27] J. Crawford, H. Yin, A. Du, A.P. O'Mullane, Angew. Chem. Int. Ed. 61 (2022) e202201604.
[28] B. Zhou, L. Yu, W. Zhang, et al., Angew. Chem. Int. Ed. 63 (2024) e202406046.
[29] G.A. Cerrón-Calle, A.S. Fajardo, C.M. Sánchez-Sánchez, S. Garcia-Segura, Appl. Catal. B: Environ. 302 (2022) 120844.
[30] Z. Zhang, M. Liu, B. Ge, et al., Chin. Chem. Lett. 36 (2025) 110657.
[31] A. Wu, C. Hong, H. Zheng, W. Teng, Chin. Chem. Lett. 36 (2025) 111066.
[32] L. Xu, L. Liu, G. Chen, D. Xia, Chin. Chem. Lett. 37 (2026) 111188.
[33] D. Liu, W. Guo, G. Mei, et al., Chin. Chem. Lett. 36 (2025) 110578.
[34] M. Xie, S. Tang, Z. Li, et al., J. Am. Chem. Soc. 145 (2023) 13957–13967.
[35] W. Siriwatcharapiboon, Y. Kwon, J. Yang, et al., ChemElectroChem 1 (2014) 172–179.
[36] H. Lin, J. Wei, Y. Guo, et al., Adv. Funct. Mater. 34 (2024) 2409696.
[37] Z. Bao, J. Zhao, S. Zhang, et al., Nano Res. 16 (2023) 9050–9058.
[38] X. Chen, R. Lu, C. Li, et al., Nat. Commun. 16 (2025) 1927.
[39] H. Wan, A. Bagger, J. Rossmeisl, Angew. Chem. Int. Ed. 60 (2021) 21966–21972.
[40] M. Karamad, T.J. Goncalves, S. Jimenez-Villegas, I.D. Gates, S. Siahrostami, Faraday Discuss 243 (2023) 502–519.
[41] M. Colombo, I. Nova, E. Tronconi, Catal. Today 197 (2012) 243–255.
[42] Q. Wei, Y. He, G. Ding, et al., Chem. Eng. J. 508 (2025) 161014.
[43] J. Wei, G. Ye, H. Lin, et al., J. Colloid Interface Sci. 670 (2024) 798–807.
[44] Y. Li, J. Wei, H. Lin, et al., ACS Catal. 15 (2025) 1672–1683.
[45] X. Zheng, Y. Yan, X. Li, Y. Liu, Y. Yao, J. Hazard. Mater. 446 (2023) 130679.
[46] Y. Zeng, C. Priest, G. Wang, G. Wu, Small Methods 4 (2020) 2000672.
[47] D. Liu, L. Qiao, S. Peng, et al., Adv. Funct. Mater. 33 (2023) 2303480.
[48] X. Zhang, Y. Wang, C. Liu, et al., Chem. Eng. J. 403 (2021) 126269.
[49] X. Fu, J. Zhang, Y. Kang, Chem Catal. 2 (2022) 2590–2613.
[50] M. Gholinejad, F. Khosravi, M. Afrasi, J.M. Sansano, C. Nájera, Catal. Sci. Technol. 11 (2021) 2652–2702.
[51] M.R. Gennero de Chialvo, A.C. Chialvo, Electrochim. Acta 44 (1998) 841–851.
[52] Y. Zhang, X. Chen, W. Wang, L. Yin, J.C. Crittenden, Appl. Catal. B: Environ. 310 (2022) 121346.
[53] J. Li, G. Zhan, J. Yang, et al., J. Am. Chem. Soc. 142 (2020) 7036–7046.
[54] J. Gao, B. Jiang, C. Ni, Y. Qi, X. Bi, Chem. Eng. J. 382 (2020) 123034.
[55] J. Zhang, H. Zhang, Y. Wu, et al., J. Mater. Chem. A 10 (2022) 5743–5757.
[56] R. Liu, H. Zhao, X. Zhao, et al., Environ. Sci. Technol. 52 (2018) 9992–10002.
[57] J.X. Liu, D. Richards, N. Singh, B.R. Goldsmith, ACS Catal. 9 (2019) 7052–7064.
[58] P. Li, Z. Jin, Z. Fang, G. Yu, Energy Environ. Sci. 14 (2021) 3522–3531.
[59] E. Pérez-Gallent, M.C. Figueiredo, I. Katsounaros, M.T.M. Koper, Electrochim. Acta 227 (2017) 77–84.
[60] Y. Wang, A. Xu, Z. Wang, et al., J. Am. Chem. Soc. 142 (2020) 5702–5708.
[61] T. Hu, C. Wang, M. Wang, C.M. Li, C. Guo, ACS Catal. 11 (2021) 14417–14427.
[62] D. De, J.D. Englehardt, E.E. Kalu, J. Electrochem. Soc. 147 (2000) 4573.
[63] K. Tada, K. Shimazu, J. Electroanal. Chem. 577 (2005) 303–309.
[64] S. Goldstein, D. Behar, T. Rajh, J. Rabani, Phys. Chem. A 120 (2016) 2307–2312.
[65] A.C.A. de Vooys, G.L. Beltramo, B. van Riet, J.A.R. van Veen, M.T.M. Koper, Electrochim. Acta 49 (2004) 1307–1314.
[66] M. Duca, M.C. Figueiredo, V. Climent, et al., J. Am. Chem. Soc. 133 (2011) 10928–10939.
[67] P.L. Searle, Analyst 109 (1984) 549–568.
[68] W. Zhao, B. Liu, J. Qin, et al., ChemPhotoChem 4 (2020) 5322–5336.
[69] D. Zhao, C. Ma, Y. Li, et al., Nano Energy 142 (2025) 111237.
[70] Y. Dai, S. Li, X. Li, et al., Adv. Funct. Mater. 35 (2025) 2420282.
[71] Y. Tang, Z. Jiang, Y. Yuan, et al., Nat. Commun. 15 (2024) 9800.
[72] J.F. Su, W.F. Kuan, H. Liu, C.P. Huang, Appl. Catal. B: Environ. 257 (2019) 117909.
[73] Y. Wang, W. Zhang, W. Wen, et al., Adv. Funct. Mater. 33 (2023) 2302651.
[74] Y. Wang, S. Wang, Y. Fu, et al., Nat. Commun. 16 (2025) 897.
[75] S.E. Bae, K.L. Stewart, A.A. Gewirth, J. Am. Chem. Soc. 129 (2007) 10171–10180.
[76] D.P. Butcher, A.A. Gewirth, Nano Energy 29 (2016) 457–465.
[77] S. Hoekx, N. Daems, D. Arenas Esteban, S. Bals, T. Breugelmans, ACS Appl. Energy Mater. 7 (2024) 3761–3775.
[78] X. Fu, X. Zhao, X. Hu, et al., Appl. Mater. Today 19 (2020) 100620.
[79] Y. Xu, M. Wang, K. Ren, et al., J. Mater. Chem. A 9 (2021) 16411–16417.
[80] N. Zhou, J. Wang, N. Zhang, et al., Chin. J. Catal. 50 (2023) 324–333.
[81] K. Huang, K. Tang, M. Wang, et al., Adv. Funct. Mater. 34 (2024) 2315324.
[82] X. Sun, Y. Tuo, C. Ye, et al., Angew. Chem. Int. Ed. 60 (2021) 23614–23618.
[83] Y. Xu, C. Cheng, J. Zhu, et al., Angew. Chem. Int. Ed. 63 (2024) e202400289.
[84] W. Chen, Y. Che, J. Xia, et al., J. Am. Chem. Soc. 146 (2024) 11542–11552.
[85] L. Wu, L. Zhang, S. Liu, et al., J. Mater. Chem. A 11 (2023) 5520–5526.
[86] Y. Wang, X. Qin, M. Shao, J. Catal. 400 (2021) 62–70.
[87] Z. Ren, K. Shi, X. Feng, ACS Energy Lett. 8 (2023) 3658–3665.
[88] L. Xu, S. Chen, B. Yin, et al., ACS Nano 19 (2025) 31780–31789.
[89] Y. Fu, S. Wang, Y. Wang, et al., Angew. Chem. Int. Ed. 62 (2023) e202303327.
[90] Y. Zhao, Y. Liu, Z. Zhang, et al., Nano Energy 97 (2022) 107124.
[91] Y. Liu, X. Zhang, S. Feizpoor, et al., Adv. Mater. 38 (2025) e14840.
[92] Z. Zhang, Y. Liu, X. Su, et al., Nano Res. 16 (2023) 6632–6641.
[93] W. Gao, K. Xie, J. Xie, et al., Adv. Mater. 35 (2023) 2202952.
[94] J.Y. Fang, Q.Z. Zheng, Y.Y. Lou, et al., Nat. Commun. 13 (2022) 7899.
[95] J.K. Nørskov, T. Bligaard, A. Logadottir, et al., J. Electrochem. Soc. 152 (2005) J23.
[96] X. Long, B. Zhao, D. Liu, et al., Angew. Chem. Int. Ed. 64 (2025) e202503424.
[97] L. Wu, S. Jia, L. Zhang, et al., Sci. China Chem. 67 (2024) 1969–1975.
[98] V. Okatenko, A. Loiudice, M.A. Newton, et al., J. Am. Chem. Soc. 145 (2023) 5370–5383.
[99] Y. Xu, K. Ren, T. Ren, et al., Appl. Catal. B: Environ. 306 (2022) 121094.
[100] H. Li, S. Li, R. Guan, et al., ACS Catal. 14 (2024) 12042–12050.
[101] W. Luo, Z. Guo, L. Ye, et al., Small 20 (2024) e2311336.
[102] Y. Wang, W. Zhou, R. Jia, Y. Yu, B. Zhang, Angew. Chem. Int. Ed. 59 (2020) 5350–5354.
[103] A. Ma, X. Wu, X. Li, et al., Appl. Surf. Sci. 653 (2024) 159397.
[104] J. Li, Q. Jiang, X. Xing, et al., Adv. Sci. 11 (2024) 2404194.
[105] J. Geng, S. Ji, Nano Res. 17 (2024) 4898–4907.
[106] M. Zheng, Y. Wan, L. Yang, et al., Energy Chem. 100 (2025) 106–113.
[107] J. Yuan, Z. Xing, Y. Tang, C. Liu, ACS Appl. Mater. Interfaces 13 (2021) 52469–52478.
[108] J. Chen, Y. Yao, Y. Yan, X. Li, Y. Liu, Water Res. 272 (2025) 122959.
[109] A. Yoon, L. Bai, F. Yang, et al., Nat. Mater. 24 (2025) 762–769.
[110] T. Zhang, D. Zhang, X. Han, et al., J. Am. Chem. Soc. 140 (2018) 16936–16940.
[111] X. Li, H. Rong, J. Zhang, D. Wang, Y. Li, Nano Res. 13 (2020) 1842–1855.
[112] L. Shan, Y. Ma, S. Xu, et al., Commun. Mater. 5 (2024) 104.
[113] H. Chen, C. Zhang, L. Sheng, et al., J. Hazard. Mater. 434 (2022) 128892.
[114] T. Zhu, Q. Chen, P. Liao, et al., Small 16 (2020) 2004526.
[115] S. Zhang, J. Wu, M. Zheng, et al., Nat. Commun. 14 (2023) 3634.
[116] J. Cai, Y. Wei, A. Cao, et al., Appl. Catal. B: Environ. 316 (2022) 121683.
[117] X. Wu, M. Nazemi, S. Gupta, et al., ACS Catal. 13 (2023) 6804–6812.
[118] Q. Gao, B. Yao, H.S. Pillai, et al., Nat. Synth. 2 (2023) 624–634.
[119] J. Yu, R.T. Gao, X. Guo, et al., Angew. Chem. Int. Ed. 64 (2025) e202415975.
[120] A.J. Martín, S. Mitchell, C. Mondelli, S. Jaydev, J. Pérez-Ramírez, Nat. Catal. 5 (2022) 854–866.
[121] Y. Wang, G. Wang, L.I. van der Wal, et al., Angew. Chem. Int. Ed. 60 (2021) 17735–17743.

[122] Y. Sun, J. Xie, Z. Fu, et al., ACS Nano 17 (2023) 13974–13984.
[123] L. Wu, J. Feng, L. Zhang, et al., Angew. Chem. Int. Ed. 62 (2023) e202307952.
[124] J. Yu, Y. Qin, X. Wang, et al., Nano Energy 103 (2022) 107705.
[125] O. Brylev, M. Sarrazin, L. Roué, D. Bélanger, Electrochim. Acta 52 (2007) 6237–6247.
[126] W. Zheng, L. Zhu, Z. Yan, et al., Environ. Sci. Technol. 55 (2021) 13231–13243.
[127] J. Yan, H. Xu, L. Chang, A. Lin, D. Cheng, Nanoscale 14 (2022) 15422–15431.
[128] J. Wei, J. Wang, W. Yu, et al., Appl. Catal. B: Environ. Energy 378 (2025) 125629.
[129] J. Liu, Y. Xu, R. Duan, et al., Nat. Commun. 16 (2025) 3595.
[130] S. Liang, X. Teng, H. Xu, L. Chen, J. Shi, Angew. Chem. Int. Ed. 63 (2024) e202400206.
[131] Z.Y. Wu, M. Karamad, X. Yong, et al., Nat. Commun. 12 (2021) 2870.
[132] Y. Zhou, R. Duan, H. Li, et al., ACS Catal. 13 (2023) 10846–10854.
[133] M. Zhang, X. Cheng, Y. Duan, et al., Adv. Funct. Mater. 35 (2025) 2413070.
[134] Z. Shen, G. Chen, X. Cheng, et al., Sci. Adv. 10 (2024) eadm9325.
[135] H. Chen, Z. Zhang, Y. Li, et al., Chem. Eng. J. 481 (2024) 148596.
[136] J.M. McEnaney, S.J. Blair, A.C. Nielander, et al., ACS Sustain. Chem. Eng. 8 (2020) 2672–2681.
[137] Z. Chen, X. Duan, W. Wei, S. Wang, B.J. Ni, J. Mater. Chem. A 7 (2019) 14971–15005.
[138] T. Zehra, M. Kaseem, S. Hossain, Y.G. Ko, Metals 11 (2021) 1182.
[139] R. Zhang, C. Li, H. Cui, et al., Nat. Commun. 14 (2023) 8036.
[140] N. Danilovic, R. Subbaraman, D. Strmcnik, et al., Angew. Chem. Int. Ed. 51 (2012) 12495–12498.
[141] K. Chandra Majhi, H. Chen, A. Batool, et al., Angew. Chem. Int. Ed. 64 (2025) e202500167.
[142] Y. Wang, F. Hao, H. Xu, et al., Angew. Chem. Int. Ed. 64 (2025) e202508617.
[143] S. Ureta-Zañartu, C. Yáñez, Electrochim. Acta 42 (1997) 1725–1731.
[144] G.E. Dima, A.C.A. de Vooys, M.T.M. Koper, J. Electroanal. Chem. 554-555 (2003) 15–23.
[145] W. Wang, J. Chen, E.C.M. Tse, J. Am. Chem. Soc. 145 (2023) 26678–26687.
[146] Q. Hu, K. Yang, O. Peng, et al., J. Am. Chem. Soc. 146 (2024) 668–676.
[147] S. Meng, Y. Ling, M. Yang, et al., Environ. Chem. Eng. 11 (2023) 109418.
[148] I. Katsounaros, G. Kyriacou, Electrochim. Acta 52 (2007) 6412–6420.
[149] Y. Lan, J. Chen, H. Zhang, W.X. Zhang, J. Yang, J. Mater. Chem. A 8 (2020) 15853–15863.
[150] Z. Guo, C. Ye, Y. Shen, J. Electroanal. Chem. 957 (2024) 118143.
[151] W. Wen, S. Fang, Y. Zhou, et al., Angew. Chem. Int. Ed. 63 (2024) e202408382.
[152] H.A. Duarte, K. Jha, J.W. Weidner, J. Appl. Electrochem. 28 (1998) 811–817.
[153] G. Jiang, M. Peng, L. Hu, et al., Chem. Eng. J. 435 (2022) 134853.
[154] R. Zhang, X. Ma, S. Zhang, et al., Angew. Chem. Int. Ed. 64 (2025) e202507724.
[155] D. Qin, S. Song, Y. Liu, et al., Angew. Chem. Int. Ed. 62 (2023) e202304935.
[156] Y. Lin, T. Wang, L. Zhang, et al., Nat. Commun. 14 (2023) 3575.
[157] A. Li, P. Zhang, E. Kan, J. Gong, eScience 4 (2024) 100157.
[158] S. Xue, Y. Gao, B. Wang, L. Zhi, Chem Catal. 3 (2023) 100762.
[159] R. Akhter, S.S. Maktedar, J. Materiomics 9 (2023) 1196–1241.
[160] M. Zhong, K. Tran, Y. Min, et al., Nature 581 (2020) 178–183.
[161] Z. Sun, H. Yin, K. Liu, et al., SmartMat 3 (2022) 68–83.
[162] L. Xu, X. Wang, X. Hu, et al., Innovation 6 (2025) 100911.
[163] C. Ai, S. Han, X. Yang, T. Vegge, H.A. Hansen, ACS Appl. Mater. Interfaces 16 (2024) 12563–12572.
[164] J.S. Elias, N. Artrith, M. Bugnet, et al., ACS Catal. 6 (2016) 1675–1679.
[165] A. Omranpour, J. Elsner, K.N. Lausch, J. Behler, ACS Catal. 15 (2025) 1616–1634.
[166] J. Xian, S. Li, H. Su, et al., Angew. Chem. Int. Ed. 62 (2023) e202304007.
[167] M. Cong, Q. Liu, D. Wang, et al., Appl. Catal. B: Environ. Energy 351 (2024) 123941.
[168] Y. Wu, Z. Jiang, Z. Lin, Y. Liang, H. Wang, Nat. Sustain. 4 (2021) 725–730.
[169] X. Su, F. Hong, Y. Fang, Y. Wen, B. Shan, Angew. Chem. Int. Ed. 64 (2025) e202422072.